NASA Public Access
Author manuscript
Remote Sens Environ. Author manuscript; available in PMC 2019 August 01.

Published in final edited form as:
Remote Sens Environ. 2018 August ; 213: 1–17. doi:10.1016/j.rse.2018.04.054.

Assessing global surface water inundation dynamics using combined satellite information from SMAP, AMSR2 and Landsat

JINYANG DU[1], **JOHN S. KIMBALL**[1], **JOHN GALANTOWICZ**[2], **SEUNG-BUM KIM**[3], **STEVEN K. CHAN**[3], **ROLF REICHLE**[4], **LUCAS A. JONES**[1], and **JENNIFER D. WATTS**[1,5]

[1]Numerical Terradynamic Simulation Group, W.A. Franke College of Forestry & Conservation, The University of Montana, Missoula, MT 59812, United States

[2]Atmospheric and Environmental Research, Lexington, MA 02421, United States

[3]Jet Propulsion Laboratory, California Institute of Technology, Pasadena, CA 91109, United States

[4]NASA Goddard Space Flight Center, Greenbelt, MD, 20771, United States

[5]Woods Hole Research Center, Falmouth, MA, 02540, United States

Abstract

A method to assess global land surface water (*fw*) inundation dynamics was developed by exploiting the enhanced *fw* sensitivity of L-band (1.4 GHz) passive microwave observations from the Soil Moisture Active Passive (SMAP) mission. The L-band *fw* (fw_{LBand}) retrievals were derived using SMAP H-polarization brightness temperature (T_b) observations and predefined L-band reference microwave emissivities for water and land endmembers. Potential soil moisture and vegetation contributions to the microwave signal were represented from overlapping higher frequency T_b observations from AMSR2. The resulting fw_{LBand} global record has high temporal sampling (1–3 days) and 36-km spatial resolution. The fw_{LBand} annual averages corresponded favourably (R=0.85, $p\text{-}value$<0.001) with a 250-m resolution static global water map (MOD44W) aggregated at the same spatial scale, while capturing significant inundation variations worldwide. The monthly fw_{LBand} averages also showed seasonal inundation changes consistent with river discharge records within six major US river basins. An uncertainty analysis indicated generally reliable fw_{LBand} performance for major land cover areas and under low to moderate vegetation cover, but with lower accuracy for detecting water bodies covered by dense vegetation. Finer resolution (30-m) fw_{LBand} results were obtained for three sub-regions in North America using an empirical downscaling approach and ancillary global Water Occurrence Dataset (WOD) derived from the historical Landsat record. The resulting 30-m fw_{LBand} retrievals showed favourable spatial accuracy for water (commission error 31.46%, omission error 30.20%) and land (commission error 0.87%, omission error 0.96%) classifications and seasonal wet and dry periods when compared to independent water maps derived from Landsat-8 imagery. The new fw_{LBand} algorithms and continuing SMAP and AMSR2 operations provide for near real-time, multi-scale monitoring of global surface water inundation dynamics and potential flood risk.

jinyang.du@ntsg.umt.edu.

NASA Author Manuscript
NASA Author Manuscript
NASA Author Manuscript

NASA Author Manuscript NASA Author Manuscript NASA Author Manuscript

Keywords

SMAP; Landsat; AMSR2; surface water inundation; flood risk

1. INTRODUCTION

The fractional cover of land surface water (*fw*) inundation is a key component of the global water budget and a controlling factor in hydrology, climate and ecosystem modelling (Pham-Duc et al., 2017; Melton et al., 2013; Watts et al., 2014). The *fw* dynamics reflect spatial and temporal changes in a number of environmental factors including anomalous rainfall-driven flood events (Sun et al., 2011), seasonal thawing and snowmelt in spring (Watts et al., 2012), and longer-term environmental changes (Lin et al., 2011). Characterizing *fw* variations has become a prerequisite for improved understanding of hydrological and ecological processes (Alsdorf et al., 2007; Fu et al., 2009), while providing essential support for a broad range of applications including water resources management (Sánchez-Carrillo et al., 2004), wetland monitoring (Melton et al., 2013), vector borne disease control (Chuang et al., 2012), and flood and drought risk assessment (Komi et al., 2017). Dynamic *fw* mapping has also been used as a prerequisite for the retrievals of higher-order land surface parameters from microwave remote sensing (Jones et al., 2010; Ye et al., 2015).

Previous approaches for satellite remote sensing of global *fw* dynamics have involved relatively low-temporal frequency but fine spatial resolution (10–100 m) *fw* mapping from optical and/or infrared (IR) imagery (Brakenridge and Anderson, 2006; Carroll et al., 2009; Verpoorter et al., 2014) or radar backscatter data (Bourgeau-Chavez et al., 2001; Bartsch et al., 2012; Kim et al., 2016). Passive microwave radiometry has also been used for *fw* mapping with relatively high temporal frequency (daily to 10-day) but at coarser (5 km to 25 km) spatial scales (Prigent et al., 2007; Schroeder et al., 2014; Du et al., 2016). Passive microwave sensors used for *fw* mapping include the Advanced Microwave Scanning Radiometer for the Earth Observing System (AMSR-E) (Kawanishi et al., 2003), Advanced Microwave Scanning Radiometer 2 (AMSR2) (Imaoka et al., 2012) and the Special Sensor Microwave/Imager (SSM/I) (Ferraro et al., 1996), which provide relatively high-frequency (18 GHz to 89 GHz) brightness temperature (T_b) observations.

Passive microwave remote sensing allows for global daily *fw* monitoring due to global coverage of current operational sensors, combined with strong microwave sensitivity to surface water and relative insensitivity to weather constraints. However, the resulting *fw* retrievals tend to underestimate surface water inundation extent in closed canopy areas due to the attenuation of surface microwave emissions by vegetation, with generally greater vegetation constraints for higher microwave frequencies (Du et al., 2016). Alternatively, the ESA Soil Moisture and Ocean Salinity (SMOS) (Kerr et al., 2001; Parrens et al., 2017) and NASA Soil Moisture Active Passive (SMAP) radiometers (Entekhabi et al., 2010) provide global coverage and frequent (mean 3-day) sampling, with potentially enhanced sensitivity to water signals underlying vegetation due to relatively greater canopy transmission of low frequency (L-band) microwave emissions (Entekhabi et al., 2010).

NASA Author Manuscript NASA Author Manuscript NASA Author Manuscript

Better capabilities are needed for near real-time assessment of surface water inundation dynamics at finer spatial scales commensurate with local landscape heterogeneity for monitoring extreme hydrological events (e.g. flood and droughts) and environmental changes (Fu et al., 2009; Fluet-Chouinard et al., 2015). Planned next generation satellite missions propose both high spatial and temporal resolution mapping of global surface water inundation dynamics designed for landscape assessments, including the NASA-ISRO Synthetic Aperture Radar (NISAR) and Surface Water Ocean Topography (SWOT) radar altimetry mission (Alvarez-Salazar et al., 2014; Fu and Ubelmann, 2014; Chapman et al., 2015; Prigent et al., 2016). However, other approaches have been developed for spatial downscaling of coarser resolution fw estimates from current operational passive microwave sensors (Galantowicz, 2002; Fluet-Chouinard et al., 2015; AER, 2017; Aires et al., 2017). The spatial downscaling process generally relies on the use of finer scale ancillary information, including flood potential maps derived from hydrologic analyses, to inform empirical spatial interpolation and downscaling of coarser resolution fw retrievals (Wu and Liu, 2015). Suitable downscaling methods applied to fw retrievals from available satellite passive microwave sensors allow for both near real-time and long-term global inundation mapping with high spatio-temporal resolutions.

In this investigation, we developed and tested an approach for estimating global fw dynamics using SMAP radiometer data that exploit enhanced L-band (1.4 GHz) microwave sensitivity to surface water; SMAP also provides observations at constant incidence angle and high T_b calibration accuracy (radiometric uncertainty ~1K) (Piepmeier et al., 2017) for potentially robust fw retrievals. Our algorithm approach also uses other land parameter information derived from overlapping AMSR2 higher frequency T_b observations to represent the influence of soil moisture and vegetation on the surface water signal. The resulting fw retrievals (hereby denoted as fw_{LBand}) provide global coverage with 1–3 day temporal sampling and 36-km resolution, and extend over the 19-month period from June 2015 to December 2016. Here the fw_{LBand} parameter defines the areal proportion of standing water within a 36-km SMAP grid cell. Furthermore, an empirical approach using ancillary surface water persistence information from the historical Landsat record (Pekel et al., 2016) was used to downscale the 36-km fw_{LBand} retrievals to 30-m resolution to evaluate the potential for finer landscape level monitoring of fw inundation dynamics from SMAP.

The paper continues with a presentation of the data and methods (section 2). The fw_{LBand} results were evaluated against alternative global fw maps derived from other available satellite records, while relative differences in fw cover from these products were evaluated over the global gradient in vegetation optical depth (VOD) derived from SMOS L-band T_b observations (section 3.1). The fw_{LBand} seasonal variations were evaluated against monthly river discharge measurements for selected large basins (section 3.2). The spatially downscaled fw_{LBand} results were also evaluated over other selected sub-regions in relation to independent surface water maps representing seasonal wet and dry periods obtained from Landsat-8 observations (section 3.3). Inundation dynamics derived from SMAP were compared with MODIS and Landsat results (section 3.4). A sensitivity analysis was also conducted to document expected fw_{LBand} performance for major global land cover types based on uncertainty in the underlying model assumptions and parameterizations (section 3.5). Finally, further discussion (section 4) and conclusions (section 5) were presented.

NASA Author Manuscript NASA Author Manuscript NASA Author Manuscript

2. METHODS

2.1. Algorithm Development

The fw_{LBand} algorithm was developed from a retrieval scheme originally used with AMSR-E W-band (89 GHz) T_b observations for detecting pan-Arctic inundation dynamics (Du et al., 2016). In the W-band fw (hereby denoted as fw_{WBand}) algorithm, a look-up table (LUT) was first established to provide reference microwave emissivities at 89 GHz for pure land and water endmembers under a range of global land and atmosphere conditions characterized by other AMSR-E land parameter retrievals and T_b frequency ratios (Du et al., 2016). The fw_{WBand} retrievals were then obtained on a per pixel basis by computing H-polarization (pol) difference ratio (DR) or combined H-pol and V-pol double difference ratio (DDR) T_b or emissivity deviations from reference conditions established for pure land and water endmember grid cells. A detailed description of the DR and DDR methods used for the AMSR-E fw_{WBand} retrievals are provided elsewhere (Du et al., 2016). In this study, a similar DR algorithm is used with SMAP L-band T_b observations for estimating fw_{LBand}. Here, the DR algorithm was established using a two-step procedure similar to the previous AMSR-E W-band algorithm application, but adapted for use with SMAP L-band T_b observations.

2.1.1 Algorithm Theoretical Basis

The satellite observed L-band emissivity of the land surface (e) under non-frozen and snow-free conditions can be described by the Tau-Omega model (Eq. 1) with negligible atmosphere effects considered (Mo et al., 1982; Jones et al., 2010):

$$\begin{aligned} T_{bp} &= fw \cdot e_{pw} \cdot T_w + (1 - f_w) \cdot e_{pl} \cdot T_l \\ e_{pl} &= [1 - \omega_p][1 - \gamma_p][1 + R^s_p \gamma_p] + (1 - R^s_p)\gamma_p \\ \gamma_p &= \exp[-VOD_p] \\ e_{pw} &= f(\varepsilon_w, S_r) \end{aligned} \quad (1)$$

Where subscript p denotes microwave polarization and subscripts w and l denote water and land variables, respectively; T_b is satellite observed brightness temperature; T is the effective surface temperature within the SMAP L-band penetration depth of pure land or water; fw is the fraction of open water within the sensor footprint; ω is the effective scattering albedo (Kurum, 2013); γ is the one-way microwave transmissivity of the canopy, which decreases exponentially with VOD; R^s is the effective microwave reflectivity of bare soil with surface roughness effects considered; ε_w denotes pure water permittivity, and S_r is the water surface roughness parameter. According to Eq. (1), L-band e_p is determined by microwave absorption and scattering properties of vegetation, surface soil and standing water, which are primarily represented by respective VOD, soil moisture and surface temperature conditions (Du et al., 2016).

An algorithm lookup table (LUT) of reference microwave emissivities for pure land and water endmember conditions at L-band was constructed *a priori* over a global range of

NASA Author Manuscript NASA Author Manuscript NASA Author Manuscript

vegetation and soil conditions defined by daily VOD and volumetric soil moisture (mv) retrievals from an existing AMSR (AMSR-E and AMSR2) global land parameter data record (LPDR; Du et al., 2017) (Table 1). Considering the dependence of land feature permittivity on temperature, the T_l and T_w derived from surface temperature (T_s) records of the NASA Goddard Earth Observing System Model version 5 (GEOS-5) land model (Lucchesi 2013; Chan et al., 2016a) were also used to represent the daily surface temperature influence on the fw_{LBand} estimates (Table 1). Other ancillary data were used to define suitable conditions for the fw_{LBand} retrieval, including fw derived from K-band (18.7 GHz and 23.8 GHz) AMSR2 T_b observations (hereby denoted as fw_{KBand}) (Du et al., 2017) and a MODIS IGBP land cover classification (Friedl et al., 2002). A pure land endmember condition was identified if no water presence was indicated for a 36-km SMAP grid cell by the ancillary MODIS land cover map and where minimum fractional water (<0.01) was detected by the corresponding fw_{KBand} record. A conservative 0.01 threshold was set by considering the AMSR LPDR retrieval uncertainties and fw_{KBand} positive retrieval biases (0.01 to 0.02) (Du et al., 2017). The L-band emissivity of the identified land endmembers was calculated as the ratio of SMAP 36-km T_b observations and T_l (or T_w). A collection of pure land and water endmembers was assembled from a one year (June 2015 to May 2016) record of SMAP T_b observations and T_l and T_w records; the averaged emissivity of the land endmembers for each surface condition defined in LUT was assigned as the final reference emissivity for land (e_{pl}^{ref}). The reference open water emissivity endmember (e_{pw}^{ref}) in the LUT was theoretically calculated for fresh water using the Fresnel Equations and Double-Debye dielectric model (Ulaby et al., 2014).

In this study, SMAP L-band H-polarization is used for inundation retrievals due to its larger emissivity range and higher sensitivity to water signals relative to V-polarization (Du et al., 2016). The fw_{LBand} of a given 36-km grid cell under the soil and vegetation conditions defined by the AMSR LPDR can be inferred from the SMAP observed emissivity at H-polarization and the corresponding LUT reference emissivities under the same conditions. Based on Eq. (1) and the 188 available literature (Du et al., 2016), the fw_{LBand} is determined using a Difference Ratio (DR):

$$\begin{aligned} fw_{LBond} &= \frac{(T_{bhl}^{ref} - T_{bh}^{obs})}{(T_{bhl}^{ref} - T_{bhw}^{ref})} \\ T_{bhl}^{ref} &= e_{hl}^{ref} \cdot T_l \\ T_{bhw}^{ref} &= e_{hw}^{ref} \cdot T_w \end{aligned} \quad (2)$$

Here T_w is assumed to be approximately equivalent to T_l ($T_w \approx T_l$; section 2.2.2). An alternative Double Difference Ratio (DDR) method utilizing V-pol and H-pol T_b differences $T_{bv} - T_{bh}$ for deriving fw (Du et al., 2016) was not used in the current study. The DDR shows higher retrieval uncertainties than the DR method in sparsely vegetated and barren land regions where relatively large V and H polarization differences resemble the characteristics of open water emissions (Du et al., 2016). Compared with higher microwave frequencies, the SMAP L-band T_b observations tend to have larger polarization differences due to more

NASA Author Manuscript NASA Author Manuscript NASA Author Manuscript

dielectrically transparent vegetation cover and smoother soil surface (Entekhabi et al., 2010; Huang et al., 2010). Higher noise level is expected in the $T_{bv}-T_{bh}$ observations relative to the single-channel 199 T_{bh} measurements.

2.1.2 Downscaling of fw_{LBand} Retrievals

An empirical approach is demonstrated in this study for spatial downscaling of 36-km resolution SMAP fw time series using the ancillary 30-m resolution Landsat Water Occurrence Dataset (WOD) (Pekel et al., 2016). The WOD maps represent an estimate of the inundation frequency of 30-m pixels over the globe determined from a 32-year Landsat image collection. For a given 36-km SMAP grid cell, the inundation occurrence defined from all WOD 30-m pixels within the cell is extracted and sorted in descending order. Inundation areas estimated by the 36-km fw_{LBand} retrieval are allocated sequentially, first to pixels with higher occurrence frequency, or most likely to be inundated, followed by allocations to pixels with lower occurrence frequency. The allocation stops when the area represented by 30-m open water pixels is equivalent to the fw_{LBand} coverage of the overlying SMAP grid cell or only 30-m pixels with zero water occurrences remain. This approach allows for potential 30-m resolution binary (flooded or non-flooded) inundation area maps to be defined globally at a near daily time step consistent with SMAP observations and WOD spatial coverage. However, for this study we only conducted the fw spatial downscaling and assessments for selected sub-regions and paired seasonal wet and dry snapshots.

2.2. Study Domain and Data Utilized

2.2.1 Study domain

This study focuses on SMAP fw_{Lband} retrieval over the global terrestrial domain, excluding permanent ice and snow covered areas. Six major river basins within the continental US (CONUS) were also selected for comparing the fw_{LBand} results against basin river discharge (Q) measurements (Section 2.2.3). The selections include the Sacramento, Rio Grande, Des Moines, Cumberland, Apalachicola and Minnesota basins (Fig. 1); these basins are defined by U.S. Geological Survey (USGS) hydrologic units (Seaber et al., 1987), delineated using the USGS Watershed Boundary Database (Berelson et al., 2004; WBD, 2004). For the Rio Grande, four smaller hydrologic catchments (Headwaters, Elephant Butte, Mimbres and Amistad) were examined within the larger basin, corresponding to drainage areas represented by the available river discharge measurement stations (Fig. 1). The six large river basins cover a diversity of climate, hydrologic and ecological conditions. The Apalachicola basin contains significant areas of forests with high biological diversity (White et al., 1998), while large portions of the Sacramento and Des Moines basins are dominated by croplands and intensive agriculture (Georgakakos et al., 1998). The Minnesota basin is affected by significant winter snow cover and seasonal freeze-thaw events (Cherkauer and Lettenmaier, 1999), while the Rio Grande basin is characterized by a semi-arid climate and strong vertical gradients in precipitation and vegetation (Klein and Barnett, 2003). Flow regulations by major dams across the Rio Grande (Graf, 1999), Sacramento (Singer, 2007) and Des Moines (Georgakakos et al., 1998) rivers strongly influence the observed seasonal river discharge in these basins relative to natural flow conditions.

NASA Author Manuscript NASA Author Manuscript NASA Author Manuscript

Three other sub-regions were used for quantitative comparisons between the 30-m downscaled fw_{LBand} data and independent water cover maps derived from Landsat-8 imagery. The three sub-regions (region 1 centered at −143.79°, 66.91°; region 2 centered at −93.88°, 38.89°; region 3 centered at −91.28°, 31.73°) are distributed across a North American latitudinal gradient extending from the Alaskan arctic to the US southern coastal plain (Fig. 1). Each sub-region represented a ~31,450 km^2 area consistent with the size of a single Landsat scene. The selected sub-regions included portions of the lower Mississippi River Valley that experienced major flooding during the 2015/2016 winter season (Emerton et al., 2017). A smaller area (0.1° × 0.1° rectangle centered at −91.55°, 31.27°) within region 3 was selected for evaluating the finer scale inundation patterns.

2.2.2 Datasets used for Algorithm Development

The fw_{LBand} algorithm approach developed in this study uses synergistic inputs from several different satellite data records, including SMAP, AMSR2, MODIS and Landsat. Satellite L-band (1.4 GHz), H-pol microwave T_b observations from the NASA SMAP mission provide primary information for delineating fw cover in the algorithm. Surface soil moisture conditions potentially influencing the SMAP T_b and fw retrievals were defined from the AMSR LPDR (version 2; Du et al., 2017). Daily T_s potentially influencing the SMAP T_b and fw retrievals were defined from the GEOS-5 forward processing system (De Lannoy et al., 2013; Chan et al., 2016a). A Boston University MOD12Q1 V004 MODIS 1 km IGBP land cover classification (Friedl et al., 2002) was used to identify permanent water bodies and associated surface water dominant grid cells for establishing the LUT used for the coarser SMAP fw retrievals (section 2.1.1). The global WOD is derived from a 32-year Landsat historical image archive (Pekel et al., 2016) and was used for spatial downscaling of the SMAP 36-km resolution fw_{LBand} retrievals to 30-m resolution over the selected sub-regions.

The NASA SMAP satellite provides global vertically (V) and horizontally (H) polarized microwave T_b observations over land and ocean with descending/ascending orbital equatorial crossings at 6:00 AM/PM local time extending from 31 March 2015 to the present (Entekhabi et al., 2010). The SMAP observations have enhanced microwave L-band sensitivity to surface and soil moisture conditions under low to moderate vegetation cover within approximately 5 kg/m^2 of above-ground vegetation biomass water content, relative to optical-IR and higher frequency microwave sensors (Chan et al., 2016a). For this study, we used the 19-month (June 2015 to December 2016) SMAP Level-1C half-orbit ascending and descending T_b record (SPL1CTB version 3) for mapping global fw dynamics. The SPL1CTB T_b data are provided in a 36 km resolution global EASE-Grid v2 projection similar to the native sensor footprint (Chan et al., 2016a), while the resulting fw_{LBand} record was derived in the same resolution and projection format.

The AMSR2 portion of the LPDR is temporally overlapping with SMAP observations and was used to define other environmental factors potentially affecting the SMAP fw retrievals. The LPDR exploits calibrated AMSR multi-frequency T_b observations for global daily mapping of multiple synergistic atmosphere and land parameters (Du et al., 2017). No LPDR daily retrievals are available for days with active precipitation or areas with identified

NASA Author Manuscript NASA Author Manuscript NASA Author Manuscript

X-band Radio Frequency Interference (RFI); the LPDR also excludes snow and frozen surface conditions, and large water bodies covering more than half of a 25-km grid cell (Du et al., 2017). Since the atmosphere is almost transparent to SMAP L-band observations (O'Neill et al., 2016), only LPDR VOD and mv data, which account for the influence of dynamic surface water (fw_{KBand}) variations on the microwave signal, were used to represent vegetation and soil moisture conditions in the SMAP fw_{LBand} retrievals; here, the AMSR2 X-band VOD and mv retrievals are used as a proxy for similar conditions influencing the SMAP L-band T_b observations.

The T_l processed for SMAP from GEOS-5 T_s represents the effective soil temperature within the L-band penetration depth (Holmes et al., 2012; Chan et al., 2016a) and is provided with the NASA SMAP L3 Radiometer Global Daily 36 km EASE-Grid Soil Moisture product Version 4 (SPL3SMP) (O'Neill et al., 2016). To evaluate the uncertainty associated with the assumption of $T_w \approx T_b$, alternative surface water temperature (T_{water}) inputs were tested for the fw_{LBand} retrieval. Here T_{water} was calculated using the GEOS-5 hourly surface temperature analysis (T_{surf}) averaged over each entire grid cell; surface temperature for land tiles only (T_{land}); and a static data set describing fractions of land (FR_{land}), permanent water (FR_{water}) and permanent ice (https://opendap.nccs.nasa.gov/dods/GEOS-5/fp/0.25_deg/assim).

The WOD is derived from Landsat imagery extending from 1984 to 2015 (Pekel et al., 2016). The WOD provides a consistent characterization of Landsat derived surface water inundation persistence over the historical sensor record, while open water occurrence is expressed as a percentage of the available Landsat observations over time identified as water covered (Pekel et al., 2016). The WOD data used for this study were obtained in a native 0.00025 degree resolution geographic projection format, representing approximately 30-m spatial resolution.

2.2.3 Datasets used for global fw_{LBand} validation

The fw_{LBand} results were compared with monthly Q observations for six major North American basins (Section 2.2.1), and detailed observations for selected sub-regions, including 30-m open water maps defined from Landsat-8 imagery. A global comparison of the SMAP fw_{LBand} results was conducted against other global fw, land cover and vegetation maps from the MODIS-SRTM (MOD44W) static open water database (Carroll et al., 2009), the LPDR fw_{KBand} retrievals derived from AMSR2 (Du et al., 2017), and an estimated L-band nadir VOD record included with the SMOS Level 3 (CLF31) soil moisture product (Al Bitar et al., 2017).

Monthly Q measurements (June 2015 to December 2016) were obtained from downstream stations within the six US river basins (USGS, 2001) (Fig. 1) for evaluating fw_{LBand} seasonal dynamics; here, we assume that seasonal variations in surface water storage defined from the SMAP fw record are proportional to river discharge from the major basins (Yamazaki et al., 2011; Du et al., 2016).

For validating the downscaled fw_{LBand} results and inundation dynamics, a 30-m resolution land and water mask was derived from selected Landsat-7 Enhanced Thematic Mapper Plus

NASA Author Manuscript NASA Author Manuscript NASA Author Manuscript

(ETM+), Landsat-8 Optical Land Imager (OLI) and Thermal Infrared Sensor (TIRS) scenes for each sub-region using Fmask software (version 3.3) (Zhu et al., 2015). The Fmask algorithm shows high accuracy in classifying land, water, cloud, and cloud shadow with a documented 2% omission error and 14% commission error (Zhu and Woodcock, 2014). The paired Landsat scenes acquired for each sub-region represent seasonal wet and dry conditions depicted by the Fmask classification results, and meet requirements for having less than 10% cloud coverage and best image quality as indicated in the Landsat-8 metadata files.

The SMAP derived inundation dynamics were evaluated over the lower Mississippi River Valley sub-region (region 3) by comparing the fw_{LBand} results against independent 14-day, 250-m resolution water occurrence maps (14×3D3OT; version 6.2) from the NASA MODIS near real-time global flood mapping product (https://floodmap.modaps.eosdis.nasa.gov) (Brakenridge and Anderson, 2006; Nigro et al., 2014). The 14-day MODIS flood product is derived from multiple 3-day products and has less cloud cover impacts than a single 3-day product (Nigro et al., 2014). A prior assessment of the MODIS dynamic flood record indicates that the 3-day product was successful in capturing flooded areas, with 44% of flood events classified with good, excellent or almost perfect accuracy, 23% of events classified as poor or fair, and 33% of events undetermined due to cloud contamination (Nigro et al., 2014).

The 250-m resolution MOD44W product is derived from a compilation of the SRTM (Shuttle Radar Topography Mission) Water Body dataset (SWBD) and the MODIS (MOD44C) Collection 5 (2000–2002) open water classification product (Carroll et al., 2009). The static global water body map derived from MOD44C data has a reported 2% commission error in the region between 60° and 90° N in North America relative to the National Land Cover Dataset (NLCD) (Carroll et al., 2009).

The AMSR LPDR fw_{KBand} record is capable of monitoring global water inundation dynamics (Du et al., 2017), but is expected to have different sensitivity to surface water than the SMAP fw_{LBand} retrievals owing to different sensor view geometries and frequency dependent sensitivity to surface conditions and vegetation cover. The annual mean (June 2015 – May 2016) of the descending SMOS Level 3 nadir VOD record (6:00 PM equatorial crossing time) was used in evaluating the SMAP ascending orbit fw_{LBand} record and relative differences with other fw records over the global domain. The microwave VOD parameter is a measure of the attenuation of microwave radiation by the vegetation canopy (Fernandez-Moran et al., 2017), which is a frequency-dependent function of vegetation water content (VWC) (Jackson and Schmugge, 1991; Jones et al., 2013). The Level 3 SMOS daily VOD record was derived simultaneously with soil moisture from dual polarization (H, V) and multi-angular SMOS measurements (Wigneron et al., 2007; Kerr et al., 2012), and optimized using a multi-orbit approach considering temporal auto-correlation of vegetation optical depth (Al Bitar et al., 2017).

2.2.4 Data processing

For generating the fw_{LBand} estimates, the SMAP T_b data were averaged from SPL1CTB fore-looking and aft-looking T_b observations, which were not corrected for open water

NASA Author Manuscript NASA Author Manuscript NASA Author Manuscript

effects as those processed for the SPL3SMP soil moisture retrievals. The SMAP SPL1CTB half-orbit files for each day were composited to a global 36-km EASE-Grid v2 format. For a given grid cell having multiple SPL1CTB data points represented, the data point with local solar time nearest to the SMAP orbital equatorial crossing time was selected for the daily composite, similar to the process used to derive the SMAP SPL3SMP product (Chan et al., 2016a). The above processing was carried out separately for SMAP ascending and descending orbit data. The AMSR2 LPDR VOD and mv record was reprocessed from the original 25-km EASE-Grid v1 projection format (Armstrong and Brodzik, 1995; Ashcroft and Wentz, 1999) to the SMAP 36-km EASE-Grid v2 format (Brodzik et al., 2012; Brodzik et al., 2014) using Nearest Neighbor resampling. In addition, a temporal linear interpolation approach was used to gap-fill missing daily AMSR2 LPDR grid cell observations using temporally adjacent LPDR retrievals (Kim et al., 2012). The LPDR interpolation enables the utilization of all available SMAP observations for global fw_{LBand} mapping despite possible mismatch between SMAP and AMSR2 swath coverages, though the underlying assumption of temporally linear changes of VOD and mv may lead to additional retrieval uncertainties. Due to overlapping SMAP polar orbital swaths, there is greater fw_{LBand} temporal coverage (~ 1 to 2 days) at higher latitudes (>45°) relative to the equatorial zones (~3 days).

Similar to the AMSR LPDR, the SMOS VOD and GEOS-5 T_{water} records were re-sampled to a 36-km EASE-Grid v2 format using the Nearest Neighbor method. The 1-km MODIS land cover and 250-m MOD44W data were also re-projected to the same 36 km EASE-Grid v2 format consistent with the fw_{LBand} results.

2.3. Evaluation of the fw_{LBand} Retrievals

A global fw comparison was conducted using the MOD44W static water map and one-year (June 2015 to May 2016) averages of SMAP fw_{LBand} and AMSR2 fw_{KBand} results. Quantitative metrics used to evaluate the relationships included correlation coefficient (R), root mean square difference (RMSD) and mean difference. The global inundation areas derived from MOD44W, fw_{LBand}, and fw_{KBand} annual averages were also compared under different vegetation biomass levels indicated by the SMOS VOD map.

In addition, the fw_{LBand} dynamics were examined using fw_{LBand} monthly mean values and corresponding monthly Q records for the six CONUS river basins over the 1.5-year study period (June 2015 to December 2016). To ensure consistent basin coverage in space and time, the fw_{LBand} monthly composites were generated from daily fw_{LBand} retrievals covering over 75% of a given basin area at least six times per month. Correlations between monthly Q and basin-averaged fw_{LBand} were then evaluated for each basin.

The downscaled 30-m fw_{LBand} results were validated against corresponding Landsat-8 (OLI and TIRS) based land and water classifications for the three selected sub-regions. For each sub-region, the fw_{LBand} accuracy relative to Landsat-8 in discriminating water and land pixels at 30-m resolution was summarized for two Landsat acquisition dates with contrasting dry and wet surface conditions. The metrics for accuracy assessment include commission error, omission error and overall accuracy. Considering N_{ji} represents the number of the pixels belonging to feature j but classified as feature i, the commission error for feature j is

NASA Author Manuscript NASA Author Manuscript NASA Author Manuscript

$N_{ij}/(N_{jj}+N_{ij})$, the omission error for feature j is $N_{ji}/(N_{jj}+N_{ji})$, and overall accuracy is $(N_{ii}+N_{jj})/(N_{ii}+N_{jj}+N_{ij}+N_{ji})$. No comparisons were made for pixels identified as cloud covered or cloud shadowed by the Landsat Fmask algorithm.

The downscaled results over the lower Mississippi River Valley (region 3 in Fig.1) obtained from 14-day fw_{LBand} averages from June 1, 2015 to May 31, 2016 were compared with MODIS 14-day water occurrence maps generated from the NASA near real-time flood mapping system, Landsat 8 OLI and Landsat 7 ETM+ land and water classifications derived from the Fmask algorithm. The striped data degradation areas in the ETM+ images were excluded from the analysis.

2.4. Estimation of fw_{LBand} Uncertainty

The assumption of $T_w \approx T_l$ (section 2.1.1) was evaluated by comparing differences between 15-day fw_{LBand} retrievals over July 1–15, 2015 derived using $T_w \approx T_l$ and those estimated using $T_w \approx T_{water}$. The GEOS-5 T_{water} is calculated for grid cells without permanent snow and ice as:

$$T_{water} = (T_{surf} - FR_{land} \cdot T_{land} / FR_{water}) \quad (3)$$

The 36-km fw_{LBand} algorithm uncertainties strongly depend on the accuracy of the LUT reference emissivities and AMSR2 LPDR temporal interpolation. These uncertainties were quantified by considering the standard deviation (SD) of each LUT reference emissivity and comparing fw_{LBand} results derived with and without LPDR interpolation. The emissivity SDs for pure land endmembers were acquired while assembling the global LUT (section 2.2.2). An additional process was performed for identifying water endmembers and their corresponding SDs. Pure water endmembers were assigned if the 36-km SMAP grid cells over land were designated as open water bodies in the ancillary MODIS IGBP land cover map and if the fw_{KBand} value of the nearest AMSR2 25-km grid cell was over 75%. The associated SDs derived from the water endmembers are assumed representative of the uncertainty associated with variations in water salinity and surface roughness, which are not accounted for in the theoretically calculated LUT reference values.

We assumed that the fw_{LBand} retrievals are impacted by random errors associated with the reference emissivity SDs and follow a normal distribution; we also assumed that the retrievals are affected by LPDR interpolation uncertainties. The estimated "true" fw_{LBand} retrievals were then derived using the same LUT approach, but with reference emissivity random errors subtracted and using un-interpolated LPDR inputs. The resulting algorithm uncertainties were then represented by the differences between one-year (June 2015 to May 2016) composites of the estimated "true" and baseline fw_{LBand} retrievals for the major MODIS IGBP land cover classes over the global domain. Other uncertainties associated with fw_{LBand} retrievals obscured by overlying vegetation (VOD) and the fw_{LBand} downscaling process are discussed separately (Section 4).

NASA Author Manuscript NASA Author Manuscript NASA Author Manuscript

3. RESULTS

3.1. Comparisons of fw_{LBand}, fw_{KBand} and MOD44W

The annual mean SMAP fw_{LBand} results (Fig. 2a) show similar global inundation patterns relative to the AMSR2 fw_{KBand} retrievals (Fig. 2b) and MOD44W global water map (Fig. 2c). All three products show extensive wetland complexes in northern Canada and Eurasia, and along major river systems such as the Amazon, Yangtze and Lena. The SMAP fw_{LBand} mean annual composite corresponds favorably with the MOD44W open water map (R=0.85, RMSD=0.064, p<0.001), while the SMAP retrievals are wetter, with a mean difference of 0.032. The above results are based on SMAP ascending orbit fw_{LBand} estimates while alternative estimates derived from descending orbit observations show similar, but slightly lower correspondence with MOD44W (R=0.80). Therefore, the following analysis is based on ascending results only. For temporal consistency, fw_{KBand} results derived from AMSR2 ascending orbit (equator crossing time 1:30 PM) observations were used in this study. The AMSR2 fw_{KBand} results show similar strong correspondence (R=0.81, RMSD=0.058) and a smaller mean wet difference (0.010) relative to the MOD44W record. In contrast to the static MOD44W map (Fig. 2c), significant inundation presence was detected by both the fw_{LBand} and fw_{KBand} observations in areas associated with more recent flooding during the 2015–2016 observation period, including the Mississippi river valley, South American Pampas, Ganges river delta, and lower Yangtze river valley (Fig. 2a and 2b). The high inundation levels observed by SMAP in southeastern South America and central Asia (Fig. 2a) were consistent with documented climate patterns of 2015–2016 including severer flooding in South America and abnormally wet conditions observed for central Asia (Blunden et al., 2016; Blunden et al., 2017). Comparisons were also made between SMAP fw_{LBand} and MOD44W data for five latitude zones as summarized in the Supplementary material.

The fw_{LBand} record shows large seasonal inundation variability along major river corridors, including the Amazon, Darling, Euphrates, Mekong and Yenisei (Fig. 2d). Large fw_{LBand} seasonal variations were also found over the Missouri and Mississippi basins, northern Venezuela, eastern Europe, west-central Asia, central and eastern China, the Indian sub-continent, Sahel region and southeastern Australia (Fig. 2d). The large fw_{LBand} variations in these areas are consistent with characteristic seasonal wet and dry cycles, and anomalous flooding associated with 2015–2016 El Niño–Southern Oscillation (ENSO) activity (Emerton et al., 2017).

Comparisons were also made between the fw_{Lband}, fw_{Kband} and MOD44W records for 36-km grid cells with low water fraction (MOD44W fw < 0.1). The correlation (R) between SMAP fw_{LBand} and MOD44W under these low water conditions is reduced to 0.38, while a relatively strong correlation (R=0.62) still exists between the two dynamic products fw_{LBand} and fw_{Kband}. Small water bodies may have large intra-annual and inter-annual variations (Song et al., 2014), which may contribute to the lower correspondence between dynamic and static inundation products. The retrieval errors translated from the uncertainties of reference land emissivity are proportional to the land fractional cover and larger retrieval uncertainties are also expected in regions with little water presence.

NASA Author Manuscript NASA Author Manuscript NASA Author Manuscript

The fw_{LBand}, fw_{KBand} and MOD44W results are expected to be less able to detect standing water under increasing vegetation cover due to the obstruction of satellite observations by intervening vegetation biomass. The sensitivity of the fw_{LBand} retrievals to vegetation cover is also expected to be less than the fw_{KBand} or optical-IR observations due to the greater vegetation transparency of L-band microwave emissions. The estimated global surface water inundation results were compared under different vegetation biomass conditions represented by the SMOS VOD map (Fig. 3). The fw_{LBand} results show greater surface water cover than fw_{KBand} and MOD44W under low to moderate vegetation levels, while the product differences are smaller for more densely vegetated areas (e.g. $VOD \geq 0.9$), which are mainly covered by evergreen broadleaf forests (Fig. 3b, 3c). All three surface water products show a general inundation increase with VOD in sparsely vegetated areas ($VOD < 0.2$), followed by a decline in inundation under higher VOD levels. The global fw and VOD pattern is consistent with generally sparse vegetation cover and lower inundation levels in arid climate zones, whereas the declining fw trend at higher VOD levels may reflect increasing limitations of the satellite observations to detect surface inundation in more densely vegetated areas. While the fw_{LBand} results indicate potentially enhanced L-band sensitivity to standing water under low to moderate vegetation cover, similar fw_{LBand}, fw_{KBand} and MOD44W results at higher VOD levels indicate minimal added value of the fw_{LBand} retrievals in more densely vegetated areas, including forests. These results may explain lower-than-expected inundation levels in wet tropical forest areas, including Amazonia, central Africa and Southeast Asia (e.g. Fig. 2).

3.2. Comparisons Between fw_{LBand} and River Discharge Data

River discharge (Q) and surface water inundation are integral components of the hydrological cycle and are closely connected with each other. Both Q and fw are sensitive to seasonal and inter-annual climate variations, and are affected by precipitation, evaporation and seasonal freeze/thaw transitions within a basin (McClelland et al., 2004; Watts et al., 2012). The basin-average fw_{LBand} results were compared with associated Q observations at the outlets of the six CONUS river basins examined (Fig. 1). The monthly fw_{LBand} results were significantly and positively correlated with the monthly Q observations (mean R=0.70 across the six basins) (Fig. 4). The Apalachicola river basin showed the strongest correlation (R=0.86) (Fig. 4a) among all basins examined, due to temporal consistency between river flow peaks and maximum inundation areas for this basin. Relatively low correlation (R=0.56) was found for the Des Moines river basin, where a temporal phase shift of fw_{LBand} relative to Q occurred in the summer seasons (Fig. 4c). Missing monthly fw_{LBand} estimates for the Des Moines and Minnesota basins (Fig. 4c and 4d) reflect predominantly frozen conditions in the winter months for these areas, since no fw_{LBand} retrievals were made under frozen conditions. In addition, comparisons between SMAP fw_{LBand} and river discharge data were made for Amazon river basin as described in the Supplementary material.

3.3. Comparisons between 30-m fw_{LBand} downscaled retrievals and Landsat-8 results

The downscaled fw_{LBand} retrievals exhibit spatial details of inundation patterns consistent with 30-m Landsat-8 (OLI, TIRS) observations representing seasonal dry and wet conditions within the three sub-regions (Fig. 5–7). In particular, major winter flooding events associated with 2015–2016 ENSO activity (Section 3.1; Fig.2a) in the lower Mississippi

NASA Author Manuscript NASA Author Manuscript NASA Author Manuscript

River Valley were captured by both datasets as widespread inundation was shown in the region for Jan. 16, 2016 (Fig. 7c and 7d) in contrast to the dry conditions illustrated in the Jul. 24, 2015 images (Fig. 7a and 7b). The inundation details for the selected focus area in region 3 confirm similar seasonal surface water patterns between the downscaled 30-m SMAP fw_{LBand} results and corresponding surface water maps from Landsat-8 (Fig. 8). Quantitative assessment of the fw_{LBand} downscaled data shows overall favorable agreement with the Landsat-8 results, with respective 30-m fw_{LBand} mean spatial classification accuracies of 70.71% for water and 98.99% for land pixels (Table 2). For all regions, the 30-m fw_{LBand} classification accuracy for water pixels was lower (mean accuracy 62.23%) under dry conditions than for flooded conditions (mean accuracy 79.19%). The average fw values detected by SMAP and Landsat-8 for the three regions are 3.07% and 2.92%, respectively. The fw_{LBand} results show an overall 0.15% or relative 5.1% higher estimated inundation than Landsat-8, consistent with the previous analysis (Section 3.1 and Fig. 3); however, the river channel gaps shown in the SMAP downscaled results (Fig.6a and 7a) indicate possible uncertainties associated with the fw_{LBand} retrieval and downscaling algorithms, which are discussed in Section 4.

3.4. Comparisons between Dynamic Inundation Products

To evaluate the ability of the SMAP retrievals to capture fw dynamics, comparisons were made between available Landsat water and land classifications, MODIS near real-time global flood mapping products and SMAP downscaled retrievals for the lower Mississippi River Valley sub-region. The resulting comparisons show overall similar inundation patterns and seasonal dynamics (Fig. 9) among the three products (R= 0.63 between MODIS and SMAP; 0.70 between OLI/ETM+ and SMAP; and 0.80 between MODIS and OLI/ETM+). The dry-down process from June to September 2015 as well as the Texas and Louisiana flooding event with losses exceeding one billion dollars in March 2016 (Blunden et al., 2017) are captured in the SMAP results and also represented in the Landsat classifications. All three products respond to the winter flooding of the region from December 2015 to January 2016 (Holmes et al., 2016) and show peak inundation in January 2016. Considering the presence of vast woody wetland in the region (King and Keeland, 1999), the prolonged high inundation level observed by SMAP from December 2015 to January 2016 may reflect the higher sensitivity of SMAP L-band retrievals to water under the vegetation canopy. However, the relative wet bias from SMAP over the one-year period may also reflect the inability of the algorithm to distinguish standing water from saturated surface soil conditions, leading to possible fw_{Lband} overestimation.

3.5. Uncertainty of fw_{LBand} Retrievals

The mean absolute difference between fw_{LBand} 15-day (July 1–15, 2015) retrievals derived using the GEOS-5 water temperature inputs $T_w \approx T_{water}$ and alternative algorithm assumption $T_w \approx T_s$ was found to be negligible (0.001) over the globe. These results indicate that the fw_{LBand} algorithm assumption for $T_w \approx T_l$ has a negligible impact on the global fw_{LBand} performance.

The results of the fw_{LBand} uncertainty analysis using error perturbation and un-interpolated LPDR inputs are summarized in Table 3. The overall fw estimation errors are within

NASA Author Manuscript NASA Author Manuscript NASA Author Manuscript

± 0.82% over 89.45% of the global terrestrial domain, excluding permanent snow and ice. The lowest retrieval errors (<0.6%) are indicated for forests and wetlands, while the largest uncertainty is shown for urban areas (1.13%) followed by grasslands (1.00%), closed shrublands (0.99%) and croplands (0.96%). The estimated retrieval error for wetland areas is small (0.22%) in contrast to a previous investigation of AMSR-E 89 GHz fw retrievals over the northern high latitudes, where the largest retrieval uncertainty was found for wetlands (Du et al., 2016). Similar to the analysis for the global land domain, algorithm uncertainties were also estimated on a continental-basis. The corresponding fw estimation errors slightly fluctuate around the global mean level, with the smallest uncertainty (± 0.73%) for South America and the largest error (± 0.89%) for Oceania. The above uncertainty analysis assumes that open water bodies and other land features are spatially separated within a grid cell without overlapping each other. For densely vegetated areas where standing water is obscured by overlying vegetation, the fw_{LBand} retrieval accuracy is likely degraded as implied from Fig. 3a and discussed in Section 4.

4. DISCUSSION

This investigation presents a new approach for satellite monitoring of global fw dynamics from SMAP, with enhanced L-band microwave sensitivity to surface water. This study also demonstrates potential downscaling of the SMAP fw_{LBand} retrievals using synergistic information from the Landsat historical record for finer (30-m) landscape delineation of fw inundation dynamics. The fw_{LBand} results show overall spatial consistency with MOD44W, but with major differences in regions where large seasonal variations (e.g. Sahel Belt) or flooding events (e.g. lower Mississippi River Valley) occurred that were not represented by the static water map. In particular, widespread inundation along the lower Mississippi river highlighted in the SMAP fw_{LBand} results (Fig. 2a and 2d) and also detected to a lesser extent by the AMSR2 fw_{KBand} retrievals (Fig. 2b) coincides with major 2015/2016 winter flooding events in the region from documented ENSO driven rainfall extremes (Emerton et al., 2017). The positive fw_{LBand} seasonal anomalies occurring over the Indian sub-continent (Fig. 2d) are consistent with abundant precipitation brought by the summer monsoon in this region. Of the two dynamic surface water products examined in this study, the fw_{LBand} results show generally higher inundation levels than the fw_{KBand} results (Fig. 2a and 2b), which is consistent with expected enhanced SMAP L-band sensitivity to surface water signals underlying vegetation relative to higher frequency (K-band) retrievals from AMSR2. The differences in global inundation areas estimated from MOD44W, fw_{KBand} and fw_{LBand} datasets (Fig. 3) illustrate their different capabilities in capturing water signals under varying vegetation conditions.

Generally greater fw_{LBand} inundation levels are consistent with the expected enhanced penetration ability of SMAP L-band observations relative to the AMSR2 K-band and MODIS optical-IR observations. Smaller differences among fw_{LBand}, fw_{KBand} and MOD44W in forested regions are consistent with reduced microwave sensitivity to surface water under dense vegetation. Similar to prior sensitivity studies using AMSR-E fw_{WBand} retrievals (Du et al., 2016), the SMAP fw_{LBand} accuracy may be degraded by overlying vegetation, especially in areas with higher canopy density (e.g. forests), though the lower frequency L-band observations indicate improved sampling under low to moderate VOD

NASA Author Manuscript NASA Author Manuscript NASA Author Manuscript

levels, complementing other *fw* products derived from satellite optical-IR and higher frequency microwave observations.

The fw_{LBand} results show favorable temporal correspondence with monthly river discharge measurements and reflect consistent seasonal dry and wet cycles over the six basins examined. Though strongly correlated, differences in the dynamics of *fw* extent and downstream Q measurements are also expected because Q may vary independently from surface water storage fluctuations due to river regulation (Papa et al., 2008; Landerer et al., 2010; Watts et al., 2012). The seasonal phase difference in fw_{LBand} and Q monthly time series for the Des Moines river basin (Fig. 4c) is likely caused by reservoir operations for flood risk management (Georgakakos et al., 1998). In addition, the correlation between downstream Q measurements and basin-average *fw* also depends on basin size and relative homogeneity of basin climatic and physical conditions (Du et al., 2016).

The empirical downscaling of SMAP 36-km fw_{LBand} retrievals using finer (30-m) scale surface water persistence maps from the historical Landsat record demonstrates a simple approach to incorporate coarser *fw* retrievals in delineating finer landscape level inundation. These results also demonstrate the potential added value of integrated satellite observations that leverage complementary information from different sensors; here, the downscaled fw_{LBand} record combines enhanced L-band sensitivity and global 1–3 day repeat monitoring capabilities from SMAP with finer resolution water mapping capabilities from Landsat. The frequent temporal sampling and the favorable accuracy of the downscaled 30-m fw_{LBand} results indicate the strong potential for SMAP data to contribute to more effective monitoring of surface inundation dynamics and flood risk.

Differences in *fw* patterns and associated classification accuracy between the fw_{LBand} and Landsat-8 results are influenced by several factors, including uncertainties related to fw_{LBand} and Fmask algorithms, potentially higher *fw* detection ability of SMAP over denser vegetated regions, and differences between Landsat-8 observed flooding during the 2015–2016 study period and ancillary 30-m WOD inundation patterns defined by the historical Landsat record used for fw_{LBand} downscaling. The overall positive difference of fw_{LBand} relative to the Landsat-8 results (section 3.3) may be due to higher fw_{LBand} sensitivity to surface water under low to moderate vegetation cover than the optical-IR retrievals from Landsat, and uncertainties associated with the Fmask algorithm (Zhu and Woodcock, 2014). The fw_{LBand} algorithm may also under- or over-estimate inundation areas when the predefined LUT reference emissivities deviate from “true” pure pixel emissivities. For example, the discontinuity of river channels delineated by the 30-m fw_{LBand} results (Fig. 6a and 7a) is caused by underestimated inundation within the overlying fw_{LBand} 36-km grid cells. In addition to the quantified uncertainties in the 36-km fw_{LBand} retrievals that may propagate into the downscaling process, additional errors may occur if a flooding event does not follow the same inundation likelihood of the recorded past, especially for regions having an extensive variety of surface inundation in both spatial and temporal dimensions. For example, the associated errors are expected to be larger in situations where an extreme flooding event exceeds the historical inundation record indicated from the Landsat WOD. Since the Landsat WOD generally records the occurrence of open water without overlying vegetation, potential under-canopy water detected by the fw_{LBand} may be mis-located in the

NASA Author Manuscript NASA Author Manuscript NASA Author Manuscript

downscaling process using WOD defined open water areas. The downscaling approach may be enhanced using a refined flood potential map which weights inundation by other topographic and hydrographic variables such as slope, distance from and elevation above the nearest water body, and other river network and basin boundary information (Galantowicz, 2002; AER, 2017; Fluet-Chouinard et al., 2015); the remotely sensed fw_{LBand} retrievals may also be integrated with more detailed information from hydraulic models to improve accuracy (Bates, 2012).

Inundation dynamics derived from MODIS, OLI/ETM+ and SMAP show similar temporal patterns and seasonal dynamics. The agreement between the optical and microwave remotely sensed inundations depends on the degree to which the microwave signal is affected by soil moisture, the amount of under-canopy flooding and the spatial and temporal distribution of flooded areas where scattered small water bodies or floods too short in duration may not be detected by optical sensors (Nigro et al., 2014).

The overall algorithm uncertainty estimates are within ± 0.82% (RMSD), indicating generally reliable 36-km fw_{LBand} retrievals for discriminating global surface inundation dynamics. The fw retrieval uncertainties are mainly associated with LUT reference emissivity and temporal interpolation of the ancillary AMSR LPDR. Reference LUT emissivities were derived under soil and vegetation conditions defined by LPDR X-band VOD and mv retrievals. Different from available SMOS and SMAP global land products, the AMSR LPDR retrievals account for the influence of surface water dynamics (Du et al., 2017). The LPDR mv retrievals show favorable accuracy as assessed by watershed soil moisture measurements ($0.63 \leq R \leq 0.84$), while the LPDR VOD record corresponds strongly ($R \geq 0.88$) with optical-IR derived Normalized Difference Vegetation Index (Du et al., 2017). However, the microwave soil penetration depth and VOD are frequency-dependent, and the inconsistency in orbital crossing time, observation geometry and frequency between AMSR2 and SMAP is expected to contribute uncertainty to the fw_{LBand} estimates. In particular, larger estimated retrieval uncertainties (RMSE>0.91%) (Table 3) in croplands, closed shrublands and grasslands reflect lower correspondence between soil and vegetation conditions sensed by SMAP and AMSR2 under these land cover types; thus, enhanced SMAP sensitivity to soil moisture unaccounted for by AMSR2 may lead to fw_{LBand} overestimation. The known RFI affecting both AMSR2 X-band and SMAP L-band T_b observations occurs mostly near densely populated locations and likely contributes to degraded fw_{LBand} performance over urban areas (Njoku et al., 2005; Aksoy et al., 2016).

The gridded SPL1CTB T_b data and resulting fw_{LBand} retrievals are assumed uniformly representative of the 36-km grid cells. However, the native SMAP radiometer retrievals are acquired within an approximate 36 km x 47 km elliptical footprint (Piepmeier et al., 2016) and contain T_b contributions from adjacent areas outside of the fixed Earth grid cell, which can contribute fw_{LBand} retrieval uncertainty depending on the T_b heterogeneity of the observed scene. Accordingly, fw_{LBand} temporal variations associated with sensor geolocation changes are expected for grid cells along coastlines and large lake bodies.

The algorithm uncertainty analysis in this study (section 2.4) is based on the assumption of exposed open water bodies surrounded by vegetation. Under this assumption, the lowest

NASA Author Manuscript NASA Author Manuscript NASA Author Manuscript

retrieval errors (<0.6%) are expected in forested areas due to the large contrast between high emissivity forest and low emissivity water surfaces. In contrast, the fw accuracy is expected to decrease exponentially under higher VOD levels in situations where standing water is obscured by overlying vegetation cover (Du et al., 2016). The fw signal-to-noise is more sensitive to VOD for higher microwave frequency (e.g. 89 GHz) retrievals relative to lower frequency observations (Du et al., 2016), while the SMAP fw_{LBand} results from this study show favorable performance under low to moderate VOD conditions (section 3.5). For open water under dense forests, strong microwave attenuation from the forest canopy may block the detection of underlying water signals from both L-band and higher microwave frequency observations (Fig. 3). These results are also consistent with a recent study for the Amazon basin, which shows SMOS T_b observations at lower incidence angles (e.g. 32°±5°) having shorter VOD slant paths that are more suitable to detect open water under dense forest than higher incidence angle observations (e.g. >47°±5°) (Parrens et al., 2017). The MODIS-SRTM (MOD44W) derived fw retrievals indicate similar degradation at higher VOD levels, while satellite optical-IR sensors are expected to have less sensitivity to surface water under sparse to moderate vegetation cover than microwave sensors (Smith, 1997).

5. CONCLUSIONS

Satellite mapping of global surface water inundation at high spatio-temporal resolutions are urgently needed for improving understanding of climate and disturbance related impacts on surface water storage and associated effects on land-atmosphere water, energy and carbon exchange. In this study we present a new approach to estimate and downscale fw from SMAP L-band T_b observations, incorporating ancillary information from an existing AMSR2 land parameter record and ancillary fine scale (30-m) inundation patterns derived from Landsat historical image archives.

The resulting SMAP 36-km fw_{LBand} retrievals show strong agreement (R=0.85) with a MODIS-SRTM derived static water map (MOD44W) over the global domain. The fw_{LBand} results also capture characteristic patterns and seasonal variations in open water inundation enabled by 1–3 day global repeat observations from SMAP. The fw_{LBand} retrievals also reveal anomalous regional inundation extremes consistent with documented ENSO-driven flooding that occurred during the 2015/2016 winter season. Compared to other available global fw records derived from optical-IR and higher-frequency microwave observations, the SMAP fw_{LBand} retrievals show enhanced surface water detection by exploiting the greater L-band microwave sensitivity to surface water. While dynamic inundation products derived from optical and radar observations at moderate to high resolution are becoming increasingly available (Brakenridge and Anderson, 2006; Nigro et al., 2014; Twele et al., 2016), the SMAP L-band observations provide consistent global coverage and frequent (3-day) sampling needed for more effective monitoring. These capabilities are especially valuable in areas where finer resolution retrievals from optical and radar sensors may be constrained by satellite orbital swath gaps, vegetation and cloud cover, complex terrain, and low solar illumination.

The estimated 36-km fw_{LBand} uncertainty contributed by the underlying algorithm is relatively small (within ± 0.82%) over the globe, while the actual fw_{LBand} accuracy is more

NASA Author Manuscript NASA Author Manuscript NASA Author Manuscript

strongly affected by and inversely proportional to overlying vegetation (VOD) cover. However, our results indicate that the SMAP fw_{LBand} retrievals provide enhanced surface water detection and monitoring capabilities in most areas except under dense forest cover ($VOD > 0.9$). The empirically downscaled 30-m fw_{LBand} results show favorable accuracy in discriminating land (commission error 31.46%, omission error 30.20%) and water (commission error 0.87%, omission error 0.96%) pixels relative to independent surface water classifications from Landsat-8 (OLI, TIRS) imagery, suggesting potential SMAP utility for finer landscape level flood risk assessments.

The global SMAP fw_{LBand} record and the empirical downscaling approach described in this study provide science data support for a broad range of research and application communities, while providing baseline information for future NASA satellite missions addressing surface water monitoring, including NISAR and SWOT. In particular, the dynamic fw_{LBand} record provides the potential for developing enhanced flood monitoring systems in conjunction with more detailed hydraulic modelling (Bates, 2012). The fw_{LBand} retrievals also benefit the SMAP mission by providing a more direct measure of dynamic surface water cover variations that can strongly impact SMAP T_b and soil moisture observations.

Supplementary Material

Refer to Web version on PubMed Central for supplementary material.

ACKNOWLEDGMENTS

SMAP brightness temperature data and land cover classification maps were provided courtesy of the National Snow and Ice Data Center (NSIDC) Distributed Active Archive Center (DAAC), located in Boulder, CO. https://earthdata.nasa.gov/about/daacs/daac-nsidc. River discharge data are available from the U.S. Geological Survey; Landsat-8 OLI and TIRS data are distributed by the Land Processes Distributed Active Archive Center (LP DAAC), located at USGS/EROS, Sioux Falls, SD. http://lpdaac.usgs.gov. The WBD is a coordinated effort between the United States Department of Agriculture-Natural Resources Conservation Service (USDA-NRCS), the United States Geological Survey (USGS), and the Environmental Protection Agency (EPA). The WBD was created from a variety of sources from each state and aggregated into a standard national layer for use in strategic planning and accountability. The SMOS data were obtained from the “Centre Aval de Traitement des Données SMOS” (CATDS), operated for the “Centre National d’Etudes Spatiales” (CNES, France) by IFREMER (Brest, France). This work was conducted at the University of Montana with funding from NASA (NNX14AI50G, NNX15AB59G). R. Reichle was support by SMAP Science Team funding.

REFERENCES

AER, 2017 ARC Flood Extent Depiction Algorithm Description Document, AFED Version V03R01, Doc. Rev. R03, AER document P1908-AFM-ADD-V03R01-R03, Atmospheric and Environmental Research (AER), Inc , Lexington, MA, USA .

Aires F, Miolane L, Prigent C, Pham B, Fluet-Chouinard E, Lehner B, Papa F. A global dynamic long-term inundation extent dataset at high spatial resolution derived through downscaling of satellite observations. J. Hydrometeorol. 2017; 18(5):1305–1325.

Aksoy M, Johnson JT, Misra S, Colliander A, O’Dwyer I. L-Band Radio-Frequency Interference Observations During the SMAP Validation Experiment 2012. IEEE Trans. Geosci. Remote Sens. 2016; 54(3):1323–1335.

Al Bitar A, Mialon A, Kerr Y, Cabot F, Richaume P, Jacquette E, Quesney A, Mahmoodi A, Tarot S, Parrens M, Al-yaari A, Pellarin T, Rodriguez-Fernandez N, Wigneron J-P. The Global SMOS Level 3 daily soil moisture and brightness temperature maps. Earth Syst. Sci. Data. 2017; 9(1):293–315.

NASA Author Manuscript NASA Author Manuscript NASA Author Manuscript

Alsdorf DE, Rodriguez E, Lettenmaier DP. Measuring surface water from space. Rev. Geophys. 2007; 45(2)

AlvarezSalazarO, HatchS, RoccaJ, RosenP, ShafferS, ShenY, SweetserT and XaypraseuthP, 2014, 11 Mission design for NISAR repeat-pass Interferometric SAR. *Proc. SPIE Sensors Syst. Next-Gener. Satell. Remote Sens* 92410C–92410C.

Armstrong RL, Brodzik MJ. An earth-gridded SSM/I data set for cryospheric studies and global change monitoring. Adv. Space Res. 1995; 16:155–163.

Ashcroft P, Wentz F, 1999 Algorithm Theoretical Basis Document, AMSR Level 2A Algorithm. Santa Rosa, CA , RSS Tech, Rep Vol. 121. 599B–1 .

Bartsch A, Trofaier AM, Hayman G, Sabel D, Schlaffer S, Clark DB, Blyth E. Detection of open water dynamics with ENVISAT ASAR in support of land surface modelling at high latitudes. Biogeosciences. 2012; 9:703–714.

Bates PD. Integrating remote sensing data with flood inundation models: how far have we got?. Hydrol. Process. 2012; 26(16):2515–2521.

Berelson WL, Paul AC, Jeffrey DH. Mapping hydrologic units for the national watershed boundary dataset1. J. Am. Water Resour. Assoc. 2004; 40:1231–1246.

Blunden J, Arndt DS. State of the Climate in 2015. Bull. Amer. Meteor. Soc. 2016; 97(8):Si–S275.

Blunden J, Arndt DS. State of the Climate in 2016. Bull. Amer. Meteor. Soc. 2017; 98(8):Si–S277.

Bourgeau-Chavez LL, Kasischke ES, Brunzell SM, Mudd JP, Smith KB, Frick AL. Analysis of space-borne SAR data for wetland mapping in Virginia riparian ecosystems Int. J. Remote Sens. 2001; 22:3665–3687.

Brakenridge GR, Anderson E. NATO Science Series: IV: Earth and Environmental Sciences. 2006; 72:1–12.

Brodzik MJ, and Knowles K. ., 2011 EASE-Grid 2.0 Land Cover Classifications from Boston University MODIS/Terra Land Cover Data Boulder, Colorado USA: NASA National Snow and Ice Data Center Distributed Active Archive Center. 10.5067/XR8523MC24TB.

Brodzik MJ, Billingsley B, Haran T, Raup B, Savoie MH. EASE-Grid 2.0: Incremental but Significant Improvements for Earth-Gridded Data Sets. ISPRS Int. J. Geo-Inform. 2012; 1:32–45.

Brodzik MJ, Billingsley B, Haran T, Raup B, Savoie MH. Correction: Brodzik, M. J. et al. EASE-Grid 2.0: Incremental but Significant Improvements for Earth-Gridded Data Sets. ISPRS Int. J. Geo-Inform.. 2014; 3:1154–1156.

Carroll M, Townshend J, DiMiceli C, Noojipady P, Sohlberg R. A New Global Raster Water Mask at 250 Meter Resolution. Int. J. Digital Earth. 2009; 2:291–308.

Chan SK, Bindlish R, O'Neill PE, Njoku E, Jackson T, Colliander A, Chen F, Burgin M, Dunbar S, Piepmeier J, Yueh S. Assessment of the SMAP passive soil moisture product. IEEE Trans. Geosci. Remote Sens. 2016a; 54(8):4994–5007.

Chan SK, Njoku E, Colliander A. 2016b SMAP L1C Radiometer Half-Orbit 36 km EASE-Grid Brightness Temperatures. Version 3 Boulder, Colorado USA: NASA National Snow and Ice Data Center Distributed Active Archive Center . doi:http://dx.doi.org/10.5067/E51BSP6V3KP7. [Date accessed January 1, 2017.].

Chapman B, McDonald KC, Shimada J, Rosenqvist A, Schroeder R, Hess LL. Mapping Regional Inundation with Spaceborne L-Band SAR. Remote Sens. 2015; 7:5440–5470.

Cherkauer KA, Lettenmaier DP. Hydrologic effects of frozen soils in the upper Mississippi River basin. J. Geophys. Res. Atmos. 1999; 104(D16):19599–19610.

Chuang TW, Henebry GM, Kimball JS, VanRoekel-Patton DL, Hildreth MB, Wimberly MC. Satellite microwave remote sensing for environmental modeling of mosquito population dynamics. Remote Sens. Environ. 2012; 125:147–156. [PubMed: 23049143]

De Lannoy GJ, Reichle RH, Pauwels VR. Global calibration of the GEOS-5 L-band microwave radiative transfer model over nonfrozen land using SMOS observations. J. Hydrometeorol. 2013; 14(3):765–785.

Donchyts G, Baart F, Winsemius H, Gorelick N, Kwadijk J, van de Giesen N. Earth's surface water change over the past 30 years. Nat. Clim. Chang. 2016; 6(9):810–813.

NASA Author Manuscript NASA Author Manuscript NASA Author Manuscript

Du J, Kimball JS, Jones LA, Watts JD. Implementation of satellite based fractional water cover indices in the pan-Arctic region using AMSR-E and MODIS. Remote Sens. Environ. 2016; 184:469–481.

Du J, Kimball JS, Jones LA, Kim Y, Glassy J, Watts JD. A global satellite environmental data record derived from AMSR-E and AMSR2 microwave earth observations. Earth Syst. Sci. Data. 2017; 9(2):791.doi: 10.5194/essd-9-791-2017

Emerton R, Cloke HL, Stephens EM, Zsoter E, Woolnough SJ, Pappenberger F. Complex picture for likelihood of ENSO-driven flood hazard. Nature Communications. 2017; 8:14796. . doi: 10.1038/ncomms14796

Entekhabi D, Njoku EG, O'Neill PE, Kellogg KH, Crow WT, Edelstein WN, Entin JK, Goodman SD, Jackson TJ, Johnson J. The Soil Moisture Active and Passive (SMAP) mission. Proc. IEEE. 2010; 98:704–716.

Ferraro RR, Grody NC, Weng F, Basist A. An eight-year (1987–1994) time series of rainfall, clouds, water vapor, snow cover, and sea ice derived from SSM/I measurements. Bull. Amer. Meteor. Soc. 1996; 77(5):891–905.

Fernandez-Moran R, Al-Yaari A, Mialon A, Mahmoodi A, Al Bitar A, De Lannoy G, Rodriguez-Fernandez N, Lopez-Baeza E, Kerr Y, Wigneron JP. SMOS-IC: An alternative SMOS soil moisture and vegetation optical depth product. Remote Sens. 2017; 9(5):457. . doi: 10.3390/rs9050457

Fluet-Chouinard E, Lehner B, Rebelo LM, Papa F, Hamilton SK. Development of a global inundation map at high spatial resolution from topographic downscaling of coarse-scale remote sensing data. Remote Sens. Environ. 2015; 158:348–361.

Friedl MA, McIver DK, Hodges JC, Zhang XY, Muchoney D, Strahler AH. Global land cover mapping from MODIS: algorithms and early results. Remote Sens. Environ. 2002; 83(1–2):287–302.

FuLL, AlsdorfD, RodriguezE, MorrowR, MognardN, LambinJ, VazeP and LafonT, 2009, March. The SWOT (Surface Water and Ocean Topography) mission: spaceborne radar interferometry for oceanographic and hydrological applications. *In OCEANOBS'09 Conference*

Fu LL, Ubelmann C. On the transition from profile altimeter to swath altimeter for observing global ocean surface topography. J. Atmos. Ocean Tech. 2014; 31(2):560–568.

Galantowicz J, Proc. IGARSS Toronto, ON, Canada: 2002 High-resolution flood mapping from low-resolution passive microwave satellite observations.; 14991502

Georgakakos AP, Yao H, Mullusky MG, Georgakakos KP. Impacts of climate variability on the operational forecast and management of the upper Des Moines River basin. Water Resour. Res. 1998; 34(4):799–821.

Graf WL. Dam nation: A geographic census of American dams and their large-scale hydrologic impacts. Water Resour. Res. 1999; 35(4):1305–1311.

Grant JP, Wigneron JP, De Jeu RAM, Lawrence H, Mialon A, Richaume P, Al Bitar A, Drusch M, van Marle MJE, Kerr Y. Comparison of SMOS and AMSR-E vegetation optical depth to four MODIS-based vegetation indices. Remote Sens. Environ. 2016; 172:87–100.

Holmes TR, Jackson TJ, Reichle RH, Basara JB. An assessment of surface soil temperature products from numerical weather prediction models using ground-based measurements. Water Resour. Res. 2012; 48:W02531. . doi: 10.1029/2011WR010538

Holmes Jr, R. R., Watson KM, , & Harris TE, 2016 Preliminary peak stage and streamflow data at selected US Geological Survey streamgages for flooding in the central and southeastern United States during December 2015 and January 2016 , No. 2016–1092, pp. 1–28 . US Geological Survey .

Huang S, Tsang L, Njoku EG, Chan KS. Backscattering coefficients, coherent reflectivities, and emissivities of randomly rough soil surfaces at L-band for SMAP applications based on numerical solutions of Maxwell equations in three-dimensional simulations. IEEE Trans. Geosci. Remote Sens. 2010; 48(6):2557–2568.

ImaokaK, MaedaT, KachiM, KasaharaM, ItoN, NakagawaK, 2012 Status of AMSR2 instrument on GCOM-W1. *Proc. SPIE Asia-Pacific Remote Sens*, 852815.

Jackson TJ, Schmugge T. Vegetation effects on the microwave emission of soils. Remote Sens. Environ. 1991; 36:203–212.

NASA Author Manuscript NASA Author Manuscript NASA Author Manuscript

Jones LA, Ferguson CR, Kimball JS, Zhang K, Chan STK, McDonald KC, Njoku EG, Wood EF. Satellite microwave remote sensing of daily land surface air temperature minima and maxima from AMSR-E. IEEE J. Sel. Top. Appl. Earth Obs. Remote Sens. 2010; 3:111–123.

Jones MO, Kimball JS, Jones LA. Satellite microwave detection of boreal forest recovery from the extreme 2004 wildfires in Alaska and Canada. Global Change Biol. 2013; 19(10):3111–3122.

Kawanishi TJ, Sezai T, Ito Y, Imaoka K, Takeshima T, Ishido Y, Shibata A, Miura M, Inahata H, Spencer RW. The Advanced Scanning Microwave Radiometer for the Earth Observing System (AMSR-E): NASDA's contribution to the EOS for global energy and water cycle studies. IEEE Trans. Geosci. Remote Sens. 2003; 41:184–94.

Kerr YH, Waldteufel P, Wigneron JP, Martinuzzi JAMJ, Font J, Berger M. Soil moisture retrieval from space: The Soil Moisture and Ocean Salinity (SMOS) mission. IEEE Trans. Geosci. Remote Sens. 2001; 39(8):1729–1735.

Kerr Y, Waldteufel P, Richaume P, Wigneron JP, Ferrazzoli P, Mahmoodi A, Al Bitar A, Cabot F, Gruhier C, Juglea SE. The SMOS Soil Moisture Retrieval Algorithm. IEEE Trans. Geosci. Remote Sens. 2012; 50:1384–1403.

Kim Y, Kimball JS, Zhang K, McDonald KC. Satellite detection of increasing Northern Hemisphere non-frozen seasons from 1979 to 2008: Implications for regional vegetation growth. Remote Sens. Environ. 2012; 121:472–487.

Kim SB, Oullette J, van Zyl JJ, Johnson JT. 2016. Dual-copolarized approach to detect surface water extent using L-land radar for the Soil Moisture Active Passive Mission. IEEE Trans. Geosci. Remote Sens. 54:3388–3399. . DOI: 10.1109/TGRS.2016.2517010

King SL, Keeland BD. Evaluation of reforestation in the lower Mississippi River alluvial valley. Restoration Ecology. 1999; 7(4):348–359.

Klein AG, Barnett AC. Validation of daily MODIS snow cover maps of the Upper Rio Grande River Basin for the 2000–2001 snow year. Remote Sens. Environ. 2003; 86(2):162–176.

Komi K, Neal J, Trigg MA, Diekkrüger B. Modelling of flood hazard extent in data sparse areas: a case study of the Oti River basin, West Africa. Journal of Hydrology: Regional Studies. 2017; 10:122–132.

Kurum M. Quantifying scattering albedo in microwave emission of vegetated terrain. Remote Sens. Environ. 2013; 129:66–74.

Landerer FW, Dickey JO, Güntner A. Terrestrial water budget of the Eurasian pan-Arctic from GRACE satellite measurements during 2003–2009. J. Geophys. Res. Atmos. 2010; 115:D23115.

Lin Z, Niu F, Liu H, Lu J. Hydrothermal processes of alpine tundra lakes, Beiluhe basin, Qinghai-Tibet Plateau. Cold Reg. Sci. Tech. 2011; 65:446–455.

Lucchesi R, 2013 File Specification for GEOS-5 FP, NASA GMAO Office Note, No. 4 (Version 1.0), National Aeronautics and Space Administration , Goddard Space Flight Center , Greenbelt, Maryland, USA Available online at http://gmao.gsfc.nasa.gov/pubs.

McClelland JW, Holmes RM, Peterson BJ, Stieglitz M. Increasing river discharge in the Eurasian Arctic: Consideration of dams, permafrost thaw, and fires as potential agents of change. J. Geophys, Res. 2004; 109:D18102.

Melton JR, Wania R, Hodson EL, Poulter B, Ringeval B, Spahni R, Bohn T, Avis CA, Beerling DJ, Chen G, Eliseev AV. Present state of global wetland extent and wetland methane modelling: conclusions from a model intercomparison project (WETCHIMP). Biogeosciences. 2013; 10:753–788.

Mo T, Choudhury BJ, Schmugge TJ, Wang R, Jackson TJ. A model for microwave emission from vegetation-covered fields. J. Geophys. Res. 1982; 87:1229–1237. C13.

Nigro J, Slayback D, Policelli F, , & Brakenridge GR; , 2014 NASA/DFO MODIS near real-time (NRT) global flood mapping product evaluation of flood and permanent water detection. Evaluation , Greenbelt, MD .

Njoku EG, Ashcroft P, Chan TK, Li L. Global survey and statistics of radio-frequency interference in AMSR-E land observations. IEEE Trans. Geosci. Remote Sens. 2005; 43(5):938–947.

O'Neill P, Chan S, Njoku E, Jackson T, Bindlish R. Soil Moisture Active Passive (SMAP) Algorithm Theoretical Basis Document (ATBD). SMAP Level 2 & 3 Soil Moisture (Passive),(L2_SM_P, L3_SM_P). Initial Release. 2012; 1

NASA Author Manuscript NASA Author Manuscript NASA Author Manuscript

O'Neill PE, Chan S, Njoku EG, Jackson T, , and Bindlish R. , 2016. SMAP L3 Radiometer Global Daily 36 km EASE-Grid Soil Moisture, Version 4 Boulder, Colorado USA NASA National Snow and Ice Data Center Distributed Active Archive Center 10.5067/OBBHQ5W22HME. [01/01/2017].

Papa F, Prigent C, Rossow WB. Monitoring flood and discharge variations in the large Siberian rivers from a multi-satellite technique. Surv. Geophys. 2008; 29:297–317.

Parrens M, Al Bitar A, Frappart F, Papa F, Calmant S, Crétaux JF, Wigneron JP, Kerr Y. Mapping Dynamic Water Fraction under the Tropical Rain Forests of the Amazonian Basin from SMOS Brightness Temperatures. Water. 2017; 9(5):350. . doi: 10.3390/w9050350

Pekel JF, Cottam A, Gorelick N, Belward AS. High-resolution mapping of global surface water and its long-term changes. Nature. 2016; 540:418–422. . DOI: 10.1038/nature20584 [PubMed: 27926733]

Pham-Duc B, Prigent C, Aires F, Papa F. Comparisons of Global Terrestrial Surface Water Datasets over 15 Years. J. Hydrometeorol. 2017; 18(4):993–1007.

Piepmeier JR, Mohammed PN, Peng J, Kim E, De Amici G, , and Ruf C; , 2016 SMAP L1B Radiometer Half-Orbit Time-Ordered Brightness Temperatures. Version 3. [Indicate subset used] Boulder, Colorado USA: NASA National Snow and Ice Data Center Distributed Active Archive Center 10.5067/YV5VOWY5V446.

Piepmeier JR. SMAP L-Band Microwave Radiometer: Instrument Design and First Year on Orbit. IEEE Trans. Geosci. Remote Sens. 2017; 55:1954–1966. . DOI: 10.1109/TGRS.2016.2631978

Prigent C, Papa F, Aires F, Rossow WB, Matthews E. Global inundation dynamics inferred from multiple satellite observations, 1993–2000. J. Geophys. Res. 2007; 112:D12107.

Prigent C, Lettenmaier DP, Aires F, Papa F. Toward a high-resolution monitoring of continental surface water extent and dynamics, at global scale: from GIEMS (Global Inundation Extent from Multi-Satellites) to SWOT (Surface Water Ocean Topography). Surv. Geophys. 2016; 37:339–355. 2.

Sánchez-Carrillo S, Angeler DG, Sánchez-Andrés R, Alvarez-Cobelas M, Garatuza-Payán J. Evapotranspiration in semi-arid wetlands: relationships between inundation and the macrophyte-cover: open-water ratio. Adv. Water Resour. 2004; 27(6):643–655.

Schroeder R, McDonald KC, Chapman B, Jensen K, Podest E, Tessler Z, Bohn TJ, Zimmerman R. Development and evaluation of a multi-year inundated land surface data set derived from active/passive microwave remote sensing data. Remote Sens. 2014; 7:16668–16732.

Seaber PR, Kapinos FP, and Knapp GL, 1987 Hydrologic unit maps Washington (DC): US Government Printing Office .

Singer MB. The influence of major dams on hydrology through the drainage network of the Sacramento River basin, California. River Res. Appl. 2007; 23(1):55–72.

Smith LC. Satellite remote sensing of river inundation area, stage, and discharge: A review. Hydrol. Process. 1997; 11(10):1427–1439.

Song C, Huang B, Ke L, Richards KS. Remote sensing of alpine lake water environment changes on the Tibetan Plateau and surroundings: A review. ISPRS Journal of Photogrammetry and Remote Sensing. 2014; 92:26–37.

Sun D, Yu Y, Goldberg MD. Deriving water fraction and flood maps from MODIS images using a decision tree approach. IEEE J. Sel. Top. Appl. Earth Obs. Remote Sens. 2011; 4(4):814–825.

Twele A, Cao W, Plank S, Martinis S. Sentinel-1-based flood mapping: a fully automated processing chain. Int. J. Remote Sens. 2016; 37(13):2990–3004.

Ulaby FT, Long DG, Blackwell WJ, Elachi C, Fung AK, Ruf C, Sarabandi K. , Zebker HA, and Van Zyl J, 2014 Microwave radar and radiometric remote sensing. Ann Arbor: University of Michigan Press .

Geological SurveyUS, 2001, *National Water Information System data available on the World Wide Web (Water Data for the Nation)*, accessed [April 12, 2017], at URL [http://waterdata.usgs.gov/nwis/].

Verpoorter C, Kutser T, Seekell DA, Tranvik LJ. A global inventory of lakes based on high-resolution satellite imagery. Geophys. Res. Lett. 2014; 41(8):6393–6402.

Watts JD, Kimball JS, Jones LA, Schroeder R, McDonald KC. Satellite Microwave remote sensing of contrasting surface water inundation changes within the Arctic–Boreal Region. Remote Sens. Environ. 2012; 127:223–236.

NASA Author Manuscript NASA Author Manuscript NASA Author Manuscript

Watts JD, Kimball JS, Bartsch A, McDonald KD. Surface water inundation in the boreal-Arctic: potential impacts on regional methane emissions. Environ. Res. Lett. 2014; 9:075001.

WBD, *Watershed Boundary Dataset*, 2004, (http://datagateway.nrcs.usda.gov) [Accessed 01/03/2017].

Wigneron JP, Kerr Y, Waldteufel P, Saleh K, Escorihuela MJ, Richaume P, Ferrazzoli P, De Rosnay P, Gurney R, Calvet JC, Grant JP. L-band microwave emission of the biosphere (L-MEB) model: Description and calibration against experimental data sets over crop fields. Remote Sens. Environ. 2007; 107(4):639–655.

White PS, Wilds SP, and Thunhorst GA, 1998 Regional Trends to Biological Resources-Southeast, in: Mac MJ, Opler PA; , Haecker CP, , & Doran PD. (Eds.) Status and Trends of the Nation's Biological Resources , United States Department of the Interior, United States Geological Survey , Reston, Virginia , pp.255–314 .

Wu G, Liu Y. Downscaling surface water inundation from coarse data to fine-scale resolution: Methodology and accuracy assessment. Remote Sens. 2015; 7(12):15989–16003.

Yamazaki D, Kanae S, Kim H, Oki T. A physically based description of floodplain inundation dynamics in a global river routing model. Water Resour. Res. 2011; 47(4):W04501. . doi: 10.1029/2010WR009726

Ye N, Walker JP, Guerschman J, Ryu D, Gurney RJ. Standing water effect on soil moisture retrieval from L-band passive microwave observations. Remote Sens. Environ.. 2015; 169:232–242.

Zhu Z, Woodcock CE. Continuous change detection and classification of land cover using all available Landsat data. Remote Sens. Environ.. 2014; 144:152–171.

Zhu Z, Wang S, Woodcock CE. Improvement and expansion of the Fmask algorithm: cloud, cloud shadow, and snow detection for Landsats 4–7, 8, and Sentinel 2 images. Remote Sens. Environ.. 2015; 159:269–277.

NASA Author Manuscript

NASA Author Manuscript

NASA Author Manuscript

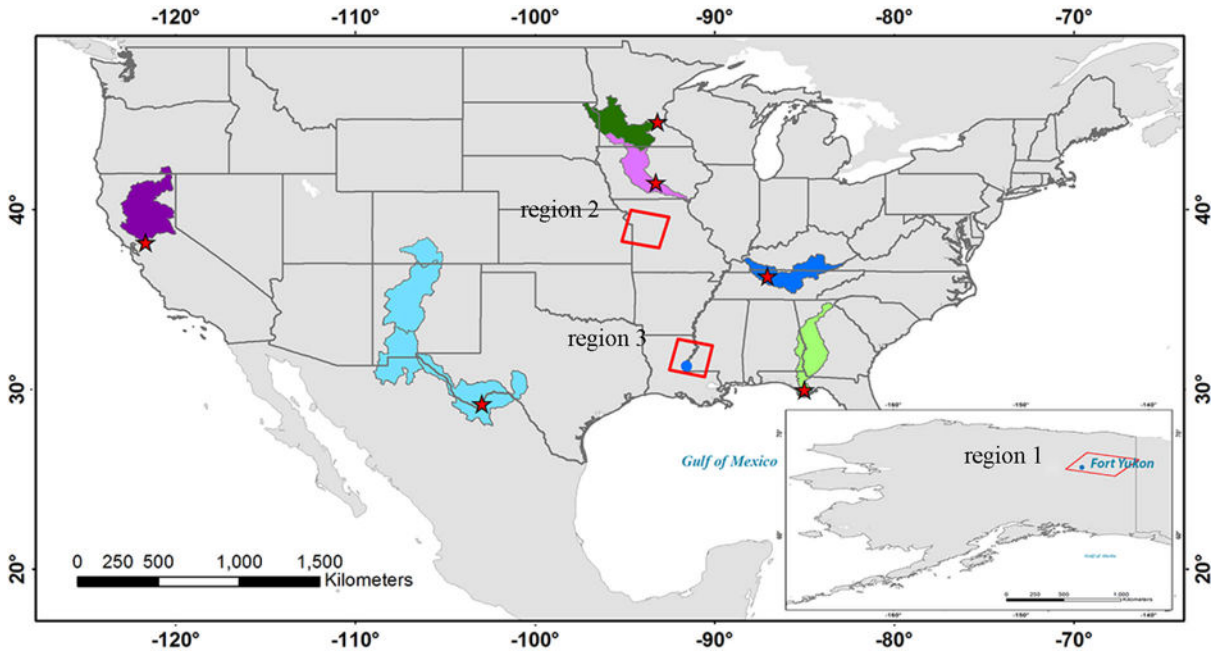

Fig.1.

Location of six river basins and three regions used in the evaluation of SMAP L-band fractional water inundation (fw_{LBand}) dynamics and fw_{LBand} downscaled results at 30-m resolution, respectively. The river basins include the Sacramento (dark purple), Des Moines (light purple), Cumberland (dark blue), Rio Grande (light blue), Minnesota (dark green) and Apalachicola (light green) basins, with river discharge stations indicated by red star symbols. The three regions (red rectangles) are defined by individual Landsat-8 image scenes, while a smaller (0.1°× 0.1°) area (blue dot) was used to highlight finer inundation details in region 3.

NASA Author Manuscript NASA Author Manuscript NASA Author Manuscript

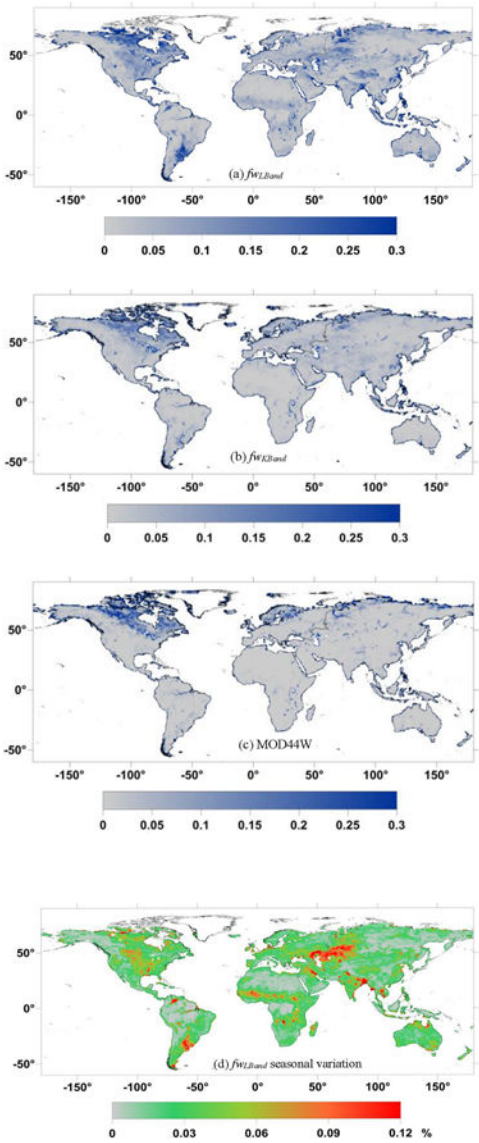

Fig.2.

Comparison of global fractional water products derived from: (a) SMAP L-band retrievals (fw_{LBand}), (b) AMSR2 K-band retrievals (fw_{KBand}), and (c) MOD44W surface water map. The SMAP fw_{LBand} and AMSR2 fw_{KBand} results represent June 2015 to May 2016 time averages, while the SMAP fw_{LBand} seasonal variation (SD) is also shown (d). The SMAP fw_{LBand} data are in a 36 km global EASE-Grid (v2) format, while the fw_{KBand} and MOD44W products were spatially aggregated from their respective 25-km and 250-m native resolutions to the same 36 km EASE (v2) grid as the fw_{LBand} results.

NASA Author Manuscript NASA Author Manuscript NASA Author Manuscript

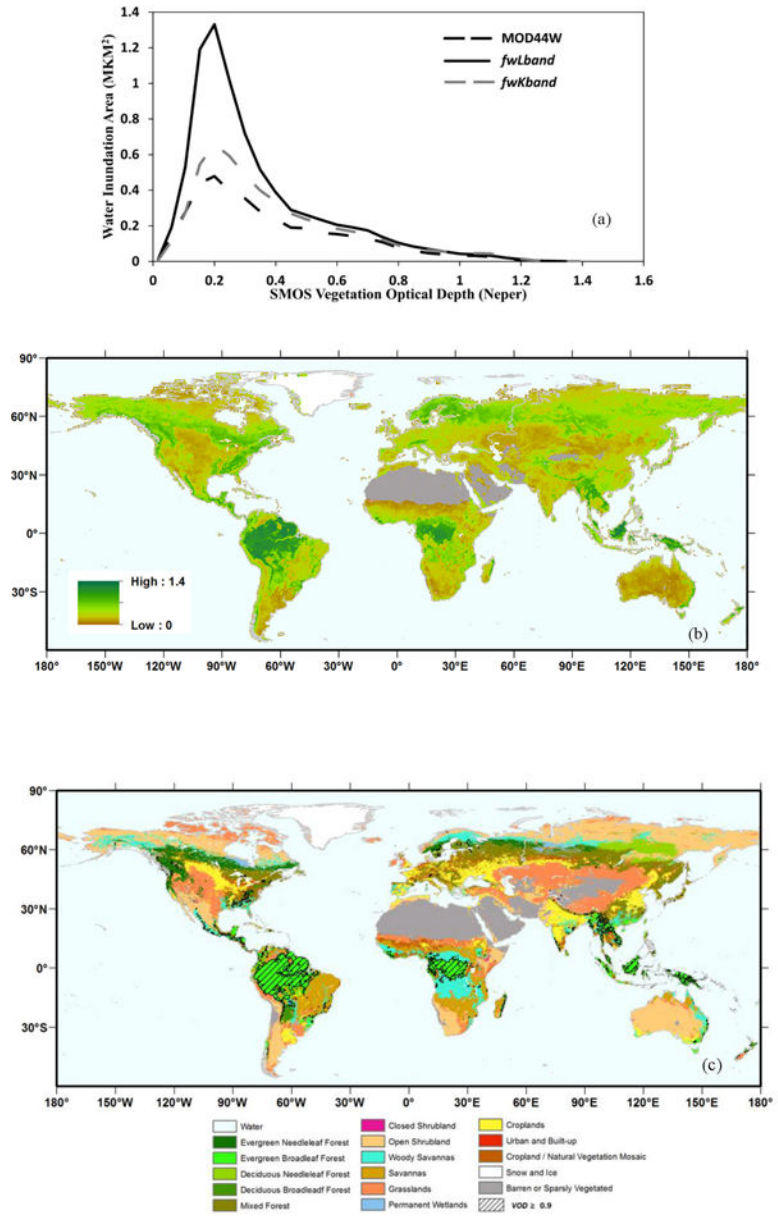

Fig.3.

Comparisons of annual mean (June 2015 to May 2016) global water inundation areas derived from MOD44W, AMSR2 fw_{KBand}, and SMAP fw_{LBand} records plotted against the global mean annual gradient in L-band vegetation optical depth (VOD) from SMOS (a). The SMOS VOD annual averages (b) were processed from the daily VOD record included in the official SMOS Level 3 soil moisture product. The VOD retrievals exclude ocean (blue), permanent snow and ice (white) and desert regions (dark grey). The MODIS IGBP global land cover map (c) is presented including regions with $VOD \geq 0.9$ (hatch patterns) where there the SMAP fw_{LBand} retrievals are degraded by dense vegetation and show no meaningful difference from the other surface water products. All products were converted to the same 36 km EASE-Grid (v2) format consistent with the fw_{LBand} and VOD results.

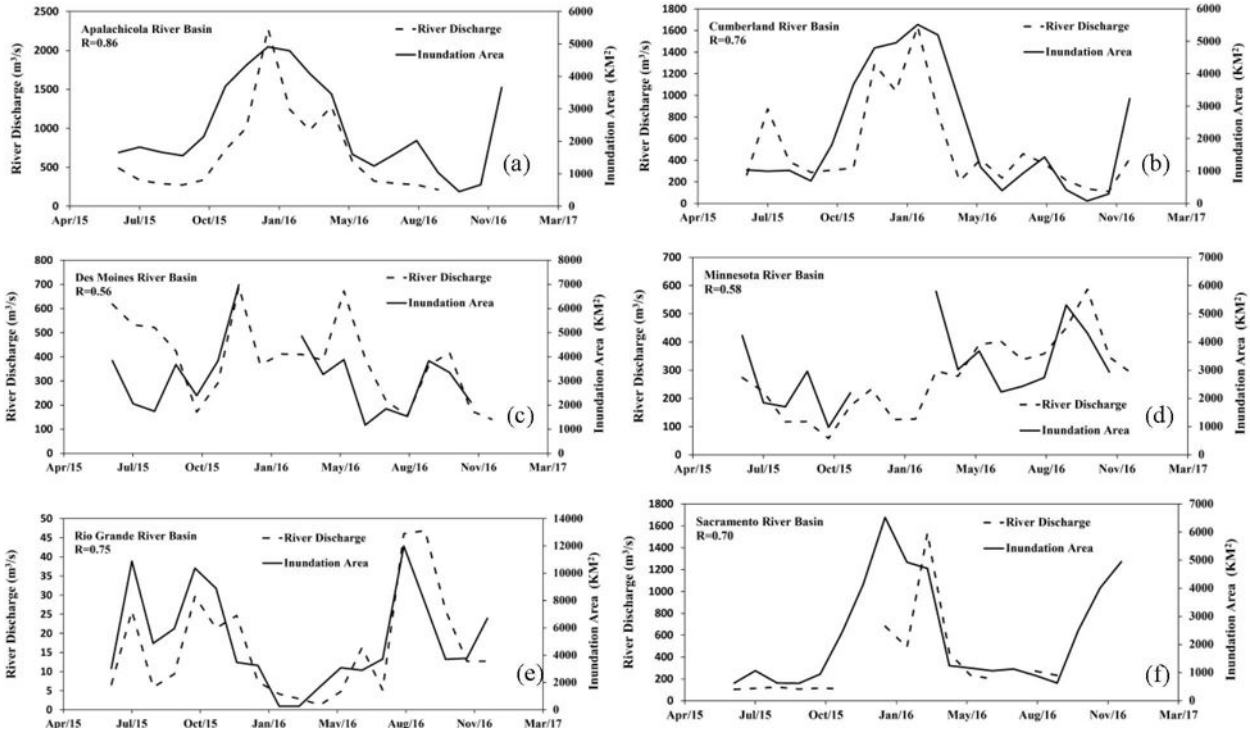

Fig.4.

Monthly mean river discharge (Q, m^3/s) and corresponding inundation areas (km^2) derived from SMAP 36 km fw_{LBand} monthly averages for the Apalachicola (a), Cumberland (b), Des Moines (c), Minnesota (d), Rio Grande (e), and Sacramento (f) river basins over the June 2015 to December 2016 record. Temporal gaps in the time series denote either missing Q observations or frozen conditions when no fw_{LBand} retrievals were made.

NASA Author Manuscript NASA Author Manuscript NASA Author Manuscript

NASA Author Manuscript NASA Author Manuscript NASA Author Manuscript

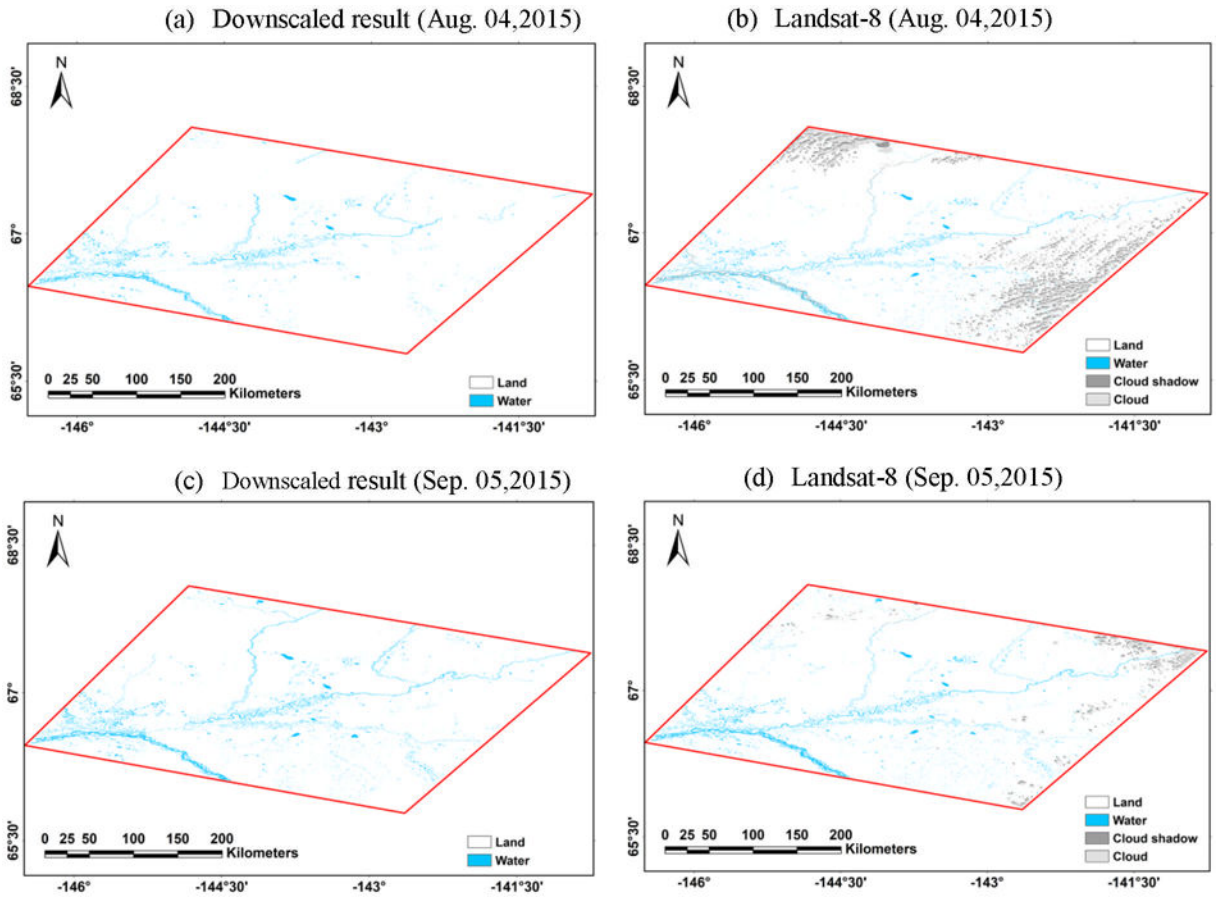

Fig.5.

SMAP downscaled results (a, c) and Landsat-8 (OLI, TIRS) (b, d) classifications of surface water (blue) and land (white) pixels for region 1 (Alaska) on Aug. 04, 2015 and Sep. 05, 2015, representing relatively dry and wet conditions. Cloud pixels in the Landsat results are marked by grey shading. SMAP classifications were based on 30-m results downscaled from the 36-km fw_{LBand} record using the climatological Landsat-based Water Occurrence Dataset. Landsat-8 classifications were derived using the Fmask algorithm (Zhu et al., 2015).

NASA Author Manuscript

NASA Author Manuscript

NASA Author Manuscript

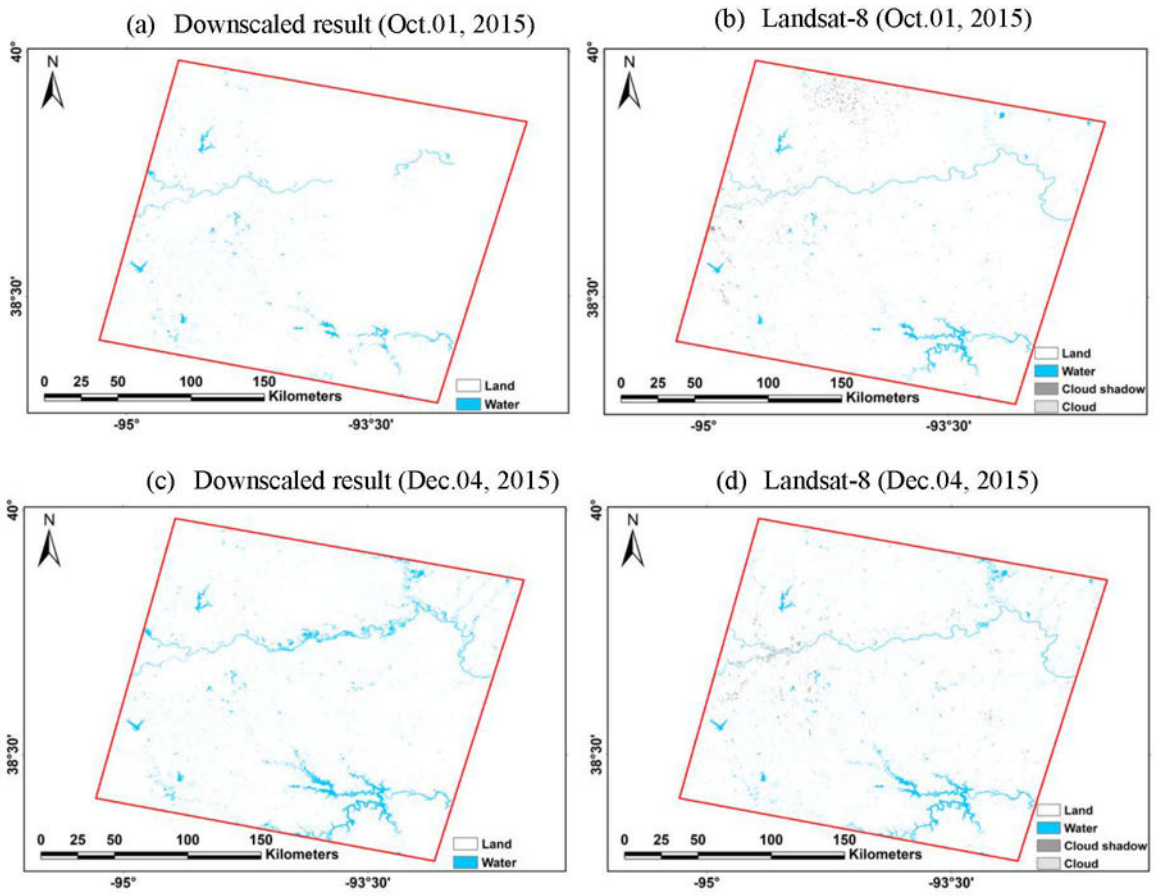

Fig.6.

SMAP downscaled results (a, c) and Landsat-8 (OLI, TIRS) (b, d) classifications of water (blue) and land (white) pixels for region 2 (western Missouri) on Oct. 01, 2015 and Dec. 04, 2015, representing relatively dry and wet conditions. Cloud pixels in the Landsat results are marked by grey shading.

NASA Author Manuscript

NASA Author Manuscript

NASA Author Manuscript

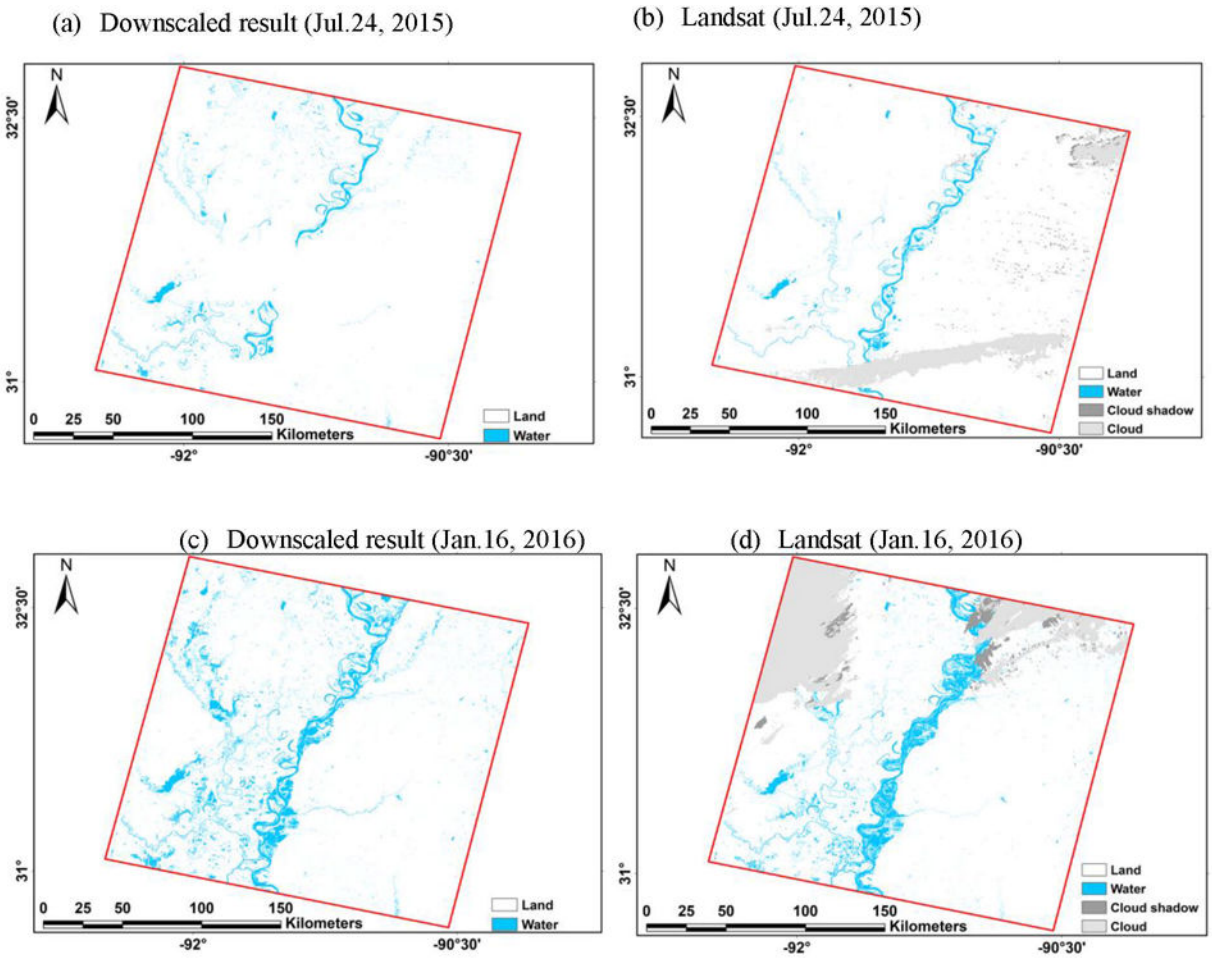

Fig.7.

SMAP downscaled results (a, c) and Landsat-8 (OLI, TIRS) (b, d) classifications of water (blue) and land (white) pixels for region 3 (lower Mississippi River Valley) on Jul. 24, 2015 and Jan. 16, 2016, representing relatively dry and wet conditions. Cloud pixels in the Landsat results are marked by grey shading.

NASA Author Manuscript

NASA Author Manuscript

NASA Author Manuscript

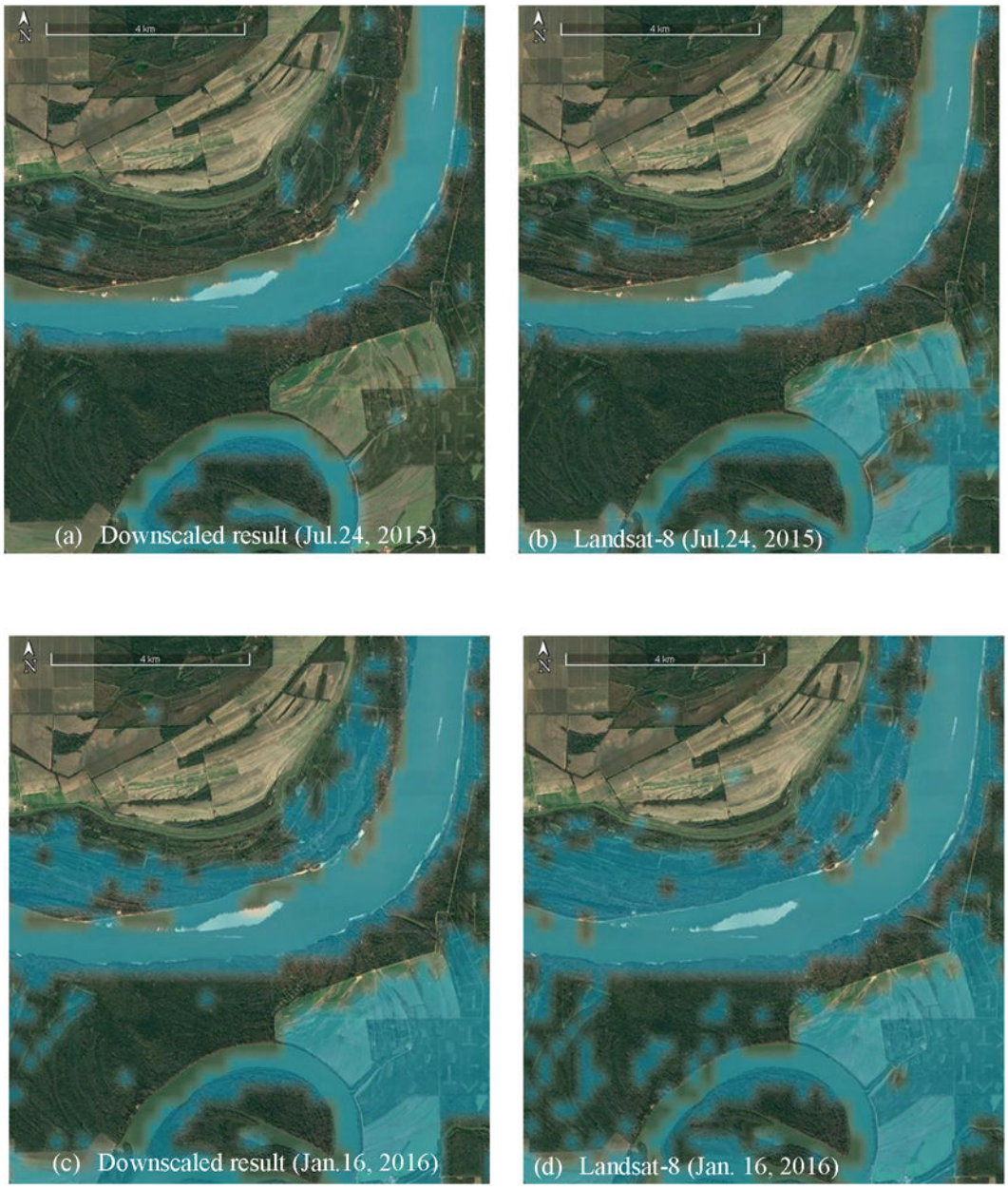

Fig.8.

SMAP downscaled results (a, c) and Landsat-8 (OLI, TIRS) (b, d) classifications of water (blue) pixels overlaid on Google Earth images (Google imagery date 12/07/2014) over a selected focus area (0.1°× 0.1° rectangle centered at −91.55°, 31.27°) within region 3 and representing respective seasonal dry and wet conditions for Jul. 24, 2015 and Jan. 16, 2016.

NASA Author Manuscript

NASA Author Manuscript

NASA Author Manuscript

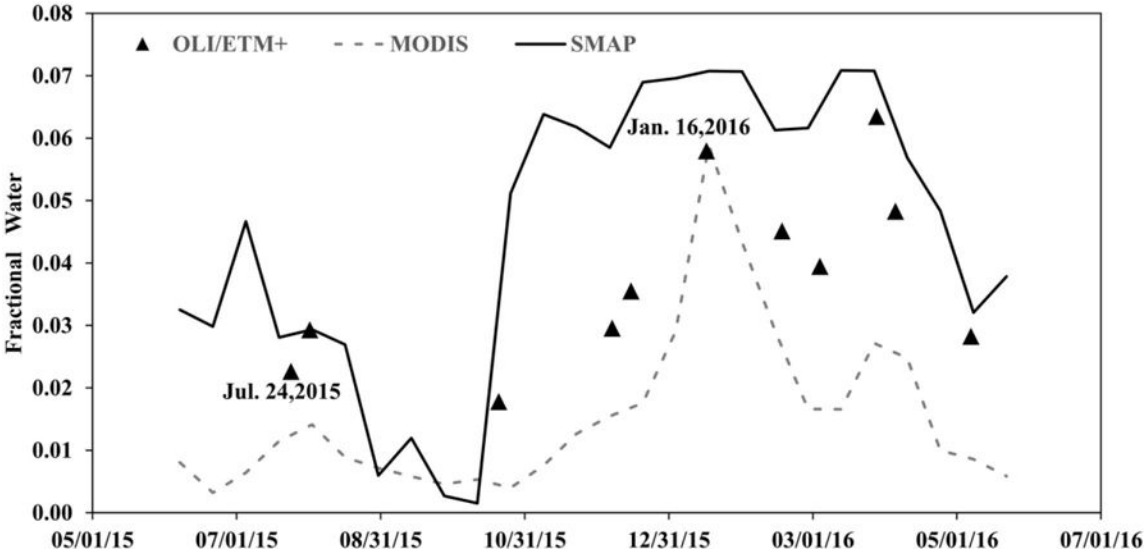

Fig.9.

Inundation dynamics derived from SMAP downscaled *fw* retrievals, the MODIS near real-time global flood mapping product, Landsat 7/ETM+ and Landsat 8/OLI water and land classifications over the lower Mississippi River Valley sub-region from June 2015 to May 2016, which encompasses a documented rainfall-driven extreme winter flood event.

NASA Author Manuscript

NASA Author Manuscript

NASA Author Manuscript

Table 1

Global land surface parameter ranges considered in the algorithm Look-up Table (LUT) used for the SMAP fw_{LBand} retrievals.

	From	To	Interval
Vegetation Optical Depth (VOD)	0.0	3.0	0.05
Volumetric Soil Moisture (Mv)	0.0 m^3/m^3	0.5 m^3/m^3	0.01 m^3/m^3
Effective soil and water surface temperature (T_l and T_w)	0 °C	42.5 °C	2.5°C

NASA Author Manuscript

NASA Author Manuscript

NASA Author Manuscript

Table 2

Water and land spatial classification accuracy of 30-m downscaled results relative to the corresponding classifications derived from Landsat-8 (OLI, TIRS) imagery.

	Land		Water		Total
Location and Date	**Commission Error**	**Omission Error**	**Commission Error**	**Omission Error**	**Overall Accuracy**
Region 1, Aug. 04, 2015	0.67%	0.54%	**29.89%**	**34.66%**	98.82%
Region 1, Sep. 05, 2015	0.57%	0.75%	**25.72%**	**20.83%**	98.72%
Region 2, Oct. 01, 2015	0.65%	0.34%	**28.78%**	**43.63%**	99.02%
Region 2, Dec. 04, 2015	0.38%	1.02%	**33.38%**	**15.53%**	98.64%
Region 3, Jul. 24, 2015	0.98%	1.20%	**44.37%**	**39.36%**	97.88%
Region 3, Jan. 16, 2016	1.96%	1.91%	**26.62%**	**27.17%**	96.40%
Overall	0.87%	0.96%	**31.46%**	**30.20%**	98.24%

NASA Author Manuscript

NASA Author Manuscript

NASA Author Manuscript

Table 3

Summary of estimated 36 km fw_{LBand} retrieval uncertainties for major global IGBP land cover types. The uncertainties are associated with the L-band LUT reference emissivity and temporal interpolation of the AMSR LPDR parameters. The original un-interpolated LPDR and random emissivity errors following a standard Normal Distribution with zero mean and Standard Deviation adopted from the LUT emissivity database were considered.

IGBP Land Cover Type	MAE *	RMSE*	Proportion*
Permanent wetlands	0.16%	0.22%	0.20%
Deciduous needleleaf forest	0.36%	0.45%	0.63%
Deciduous broadleaf forest	0.42%	0.50%	1.58%
Mixed forests	0.41%	0.52%	4.73%
Evergreen needleleaf forest	0.45%	0.58%	3.99%
Evergreen broadleaf forest	0.51%	0.59%	10.09%
Woody savannas	0.57%	0.67%	7.57%
Barren or sparsely vegetated	0.67%	0.79%	13.75%
Cropland/natural vegetation mosaic	0.75%	0.88%	2.10%
Open shrublands	0.75%	0.89%	18.42%
Savannas	0.81%	0.91%	6.99%
Croplands	0.77%	0.96%	9.03%
Closed shrublands	0.90%	0.99%	0.52%
Grasslands	0.80%	1.00%	9.33%
Urban and built-up	0.87%	1.13%	0.49%
*Overall Performance	0.67%	0.82%	89.45%

*MAE is the spatial mean absolute error; RMSE is the root mean square error; Proportion is the areal proportion of the land cover category relative to the global land domain. Overall Performance represents the statistics made for all the pixels of the listed land cover types.